PHYSICS-ALIGNED FIELD RECONSTRUCTION WITH DIFFUSION BRIDGE

Anonymous authors
Paper under double-blind review

ABSTRACT

The reconstruction of physical fields from sparse measurements is pivotal in both scientific research and engineering applications. Traditional methods are increasingly supplemented by deep learning models due to their efficacy in extracting features from data. However, except for the low accuracy on complex physical systems, these models often fail to comply with essential physical constraints, such as governing equations and boundary conditions. To overcome this limitation, we introduce a novel data-driven field reconstruction framework, termed the Physics-aligned Schrödinger Bridge (PalSB). This framework leverages a diffusion bridge mechanism that is specifically tailored to align with physical constraints. The PalSB approach incorporates a dual-stage training process designed to address both local reconstruction mapping and global physical principles. Additionally, a boundary-aware sampling technique is implemented to ensure adherence to physical boundary conditions. We demonstrate the effectiveness of PalSB through its application to three complex nonlinear systems: cylinder flow from Particle Image Velocimetry experiments, two-dimensional turbulence, and a reaction-diffusion system. The results reveal that PalSB not only achieves higher accuracy but also exhibits enhanced compliance with physical constraints compared to existing methods. This highlights PalSB's capability to generate high-quality representations of intricate physical interactions, showcasing its potential for advancing field reconstruction techniques.

1 INTRODUCTION

Field reconstruction is critically important in several domains, including fluid mechanics (Fukami et al., 2023; Manohar et al., 2018), meteorology (Carrassi et al., 2018; Kondrashov & Ghil, 2006; Tello Alonso et al., 2010), and astrophysics (The Event Horizon Telescope Collaboration, 2019), where high-fidelity data is essential. This process aims to recover the spatiotemporal information of a physical system from limited observations gathered by sensors. The challenges of measurement sparsity and noise necessitate efficient and accurate methodologies that enhance understanding of complex systems beyond the resolution capabilities of the instruments used.

However, the intrinsic challenges posed by the ill-posed nature of inverse problems and the complex spatiotemporal interactions within many systems, such as turbulence, render these reconstructions particularly difficult (Buzzicotti, 2023). Traditional physics-based methods, which repeatedly recalibrate to balance observational data with physical laws, often incur significant computational costs due to their intensive requirements for high-fidelity simulations.

Recent advances in machine learning, especially diffusion-based models, have shown promise in managing complex data distributions and have been successfully applied in diverse areas such as image translation (Zhang et al., 2023; Luo et al., 2023; Meng et al., 2022; Su et al., 2023; Yue et al., 2023), molecular generation (Xu et al., 2022; Watson et al., 2023; Igashov et al., 2024), and dynamic forecasting (Gao et al., 2023; Yoon et al., 2023; Cachay et al., 2023). Despite achieving remarkable point-wise accuracy compared to other end-to-end methods, these models often fail to align with physical laws in the context of physical field reconstruction. The challenge is exacerbated by the non-convex and often intractable nature of the domains defined by the governing physical laws, such as partial differential equations (PDEs). The projection-based methods for enforcing hard constraints (Liu et al., 2023a; Lou & Ermon, 2023; Christopher et al., 2024) are therefore inapplicable

due to the intractable domain of constraints. An alternative approach involves embedding these physical laws directly into the optimization objective as soft constraints, as seen in Physics-Informed Neural Networks (PINNs) (Raissi et al., 2019; 2020). However, this strategy can lead to severe convergence issues without appropriate initial conditions, due to the non-convex nature of these objectives (Krishnapriyan et al., 2021; Wang et al., 2022a).

In response, we propose a **P**hysics-**al**igned **S**chrödinger **B**ridge (PalSB) framework to address these challenges, ensuring both efficient and physically compliant field reconstruction. Our framework integrates a two-stage training strategy that first uses a diffusion Schrödinger bridge (DSB) for high-quality field generation from sparse measurements. This initial stage creates super-resolved fields which, while accurate, may not fully comply with physical laws. With this as a foundation, the model is further refined in the second stage through a physics-informed objective tailored to such a diffusion bridge, enhancing its adherence to physical principles. Additionally, we innovate the sampling process to ensure boundary condition compliance and to streamline generation, targeting efficiency within 10 number of function evaluations (NFEs).

Our main contributions can be summarized as follows:

- We explore the application of DSB in physical field reconstruction from sparse measurements, focusing on efficient and scalable training strategies that circumvent the need for full field data during initial training phases.
- We develop a physics-aligned fine-tuning approach for generative models to address optimization challenges associated with physics-informed loss functions, significantly improving the physical compliance of the generated fields.
- We introduce an innovative sampling technique that effectively incorporates boundary conditions into the generative process.

2 Background

Problem Setups

Given the low-fidelity measurements denoted as $\mathbf{y} \in \mathbb{R}^m$ discretized over domain $\Omega \subset \mathbb{R}^d$, the goal of field reconstruction is to recover the high-fidelity spatiotemporal field $\mathbf{x}_0 \in \mathbb{R}^n$ over the same domain. The forward mapping from $\mathbf{x}_0$ to $\mathbf{y}$ can be represented as $\mathbf{y} = \mathcal{H}(\mathbf{x}_0) + \epsilon$, where $\mathcal{H}$ is the observation operator and ϵ is the Gaussian noise introduced by measurement errors. In other words, the measurements can be regarded as a sample of conditional distribution $p(\mathbf{y}|\mathbf{x}_0) = \mathcal{N}(\mathbf{y}; \mathcal{H}(\mathbf{x}_0), {\sigma_\epsilon}^2 \mathbf{I}_m)$. To inversely acquire $\mathbf{x}_0$ from measurements $\mathbf{y}$, one need to model the posterior probability $p(\mathbf{x}_0|\mathbf{y})$ whose form is inaccessible in most scenarios. From either a paired dataset $\left\{{\mathbf{x}_0}^{(i)}, \mathbf{y}^{(i)}\right\}_{i=1}^{N}$ or a given prior distribution of $\mathbf{x}_0$, such posterior can be statistically approximated in a data-driven manner.

Diffusion Schrödinger Bridge

The Schrödinger bridge problem, stemming from optimal transport and stochastic processes (Schrödinger, 1932; Léonard, 2012; Chen et al., 2016), provides a methodological framework to efficiently transition between two probability distributions p_0 and p_1. This is achieved through the formulation of forward and backward stochastic differential equations (SDEs):

$$d\mathbf{x}_t = [\mathbf{f}(t) + \beta(t)\nabla \log \Psi(\mathbf{x}_t, t)]dt + \sqrt{\beta(t)}dW_t \tag{1a}$$

$$d\mathbf{x}_t = [\mathbf{f}(t) - \beta(t)\nabla \log \hat{\Psi}(\mathbf{x}_t, t)]dt + \sqrt{\beta(t)}d\overline{W}_t \tag{1b}$$

where $t \in [0, 1]$ is the time variable, $\mathbf{f}(t)$ represents the drift term at time t, $\beta(t)$ is the diffusion coefficient, and dW_t and $d\overline{W}_t$ are the incremental Wiener processes for the forward and backward SDEs, respectively. The functions $\Psi(\mathbf{x}_t, t)$ and $\hat{\Psi}(\mathbf{x}_t, t)$ are the forward and backward potentials guiding the transformation between p_0 and p_1. Modifying the drift term $\mathbf{f}(t)$ to $\mathbf{f}(t)' - \beta(t)\nabla \log \Psi(\mathbf{x}_t, t)$ integrates the formulation into the framework of score-based generative models (Song et al., 2021),

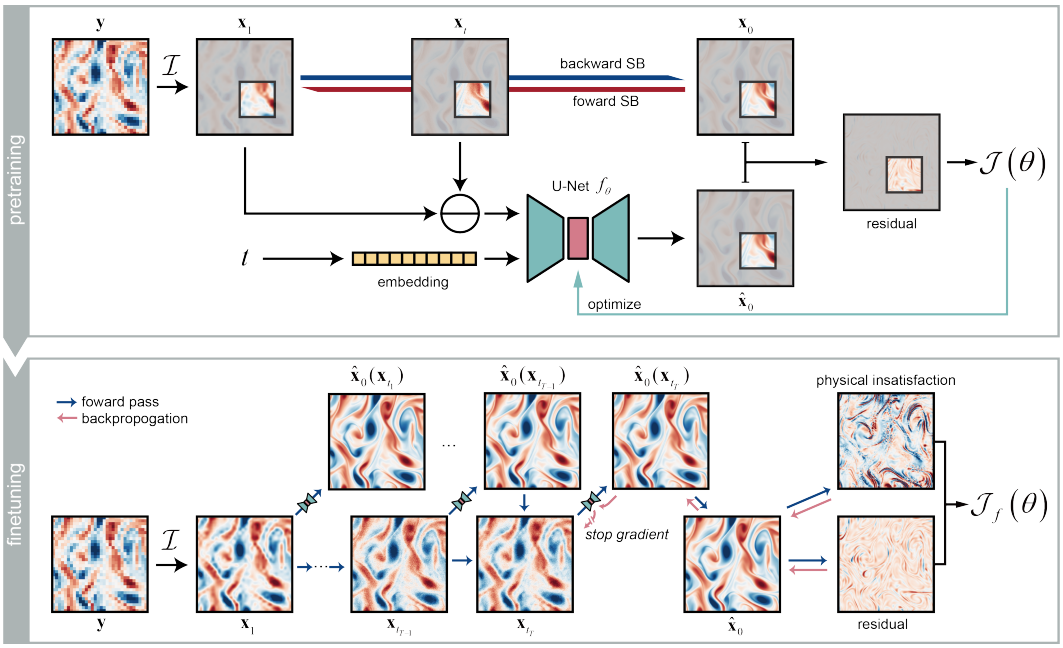

Figure 1: Work flow of PalSB. In pretraining stage (top row), the low-fidelity field $\mathbf{y}$ is first interpolated to the same grid for output and the Gaussian-perturbed linear interpolation of the paired samples is then fed into the neural network to make a prediction of the high-fidelity output, where the residual between predition and label is utilized to optimize the neural network. In finetuning stage (bottom row), leveraging the pretrained model, a prediction of high-fidelity field is sampled from the low-fidelity condition through the DSB, assessed then by two metrics that evaluate the physical loss and regression loss. Subsequently, the model is tuned through the sampling path using the weighted loss.

where the score function $\nabla \log p_t(\mathbf{x}, t) = \nabla \log[\Psi(\mathbf{x}, t)\hat{\Psi}(\mathbf{x}, t)]$ guides the evolution of the probability from data distribution p_0 to a zero-mean Gaussian p_1. Considering that the diffusion process in a DSB does not necessarily conclude at a Gaussian distribution, additional information can be injected into the final distribution p_1. When the starting and ending distributions are $p_0(\mathbf{x})$ and $p(\mathbf{y}|\mathbf{x}_0)$, respectively, the forward SDE models the degradation from high-fidelity to low-fidelity data, which can theoretically be reversed via the backward SDE once the function $\hat{\Psi}(\mathbf{x}, t)$ is determined.

Compared to vanilla diffusion models such as DDPM (Ho et al., 2020) and score SDE (Song et al., 2021), DSB is more flexible in alternating the boundary distributions, promoting the direct modeling of inverse problem without starting from pure Gaussian noise. Moreover, the optimality of DSB in transferring distributions can significantly reduce the number of sampling steps. Despite these advantages, solving the Schrödinger bridge problem is complex in practice since a close-form solution for DSB does not exist in general cases. Some methods approximate the solution using an iterative algorithm that needs to simulate the learned SDE (De Bortoli et al., 2021; Chen et al., 2022; Tang et al., 2024), while some recent studies introduce the simulation-free approaches for solving DSB (Tong et al., 2024; Liu et al., 2023b). Among these methods, the $\mathrm{I}^2$2SB approach (Liu et al., 2023b), which is simple for implementation, proposes that both potentials conform to the constraints of the probabilistic density function, resulting in corresponding score functions $\nabla \log \Psi(\mathbf{x}_t, t)$ and $\nabla \log \hat{\Psi}(\mathbf{x}_t, t)$ for the reversed paths of the described SDEs:

$$d\mathbf{x}_t = \mathbf{f}(t)dt + \sqrt{\beta(t)}dW_t, \mathbf{x}_0 \sim \hat{\Psi}(\cdot, 0) \tag{2a}$$

$$d\mathbf{x}_t = \mathbf{f}(t)dt + \sqrt{\beta(t)}d\overline{W}_t, \mathbf{x}_1 \sim \Psi(\cdot, 1) \tag{2b}$$

Given appropriate boundary distributions, the posterior distributions $\Psi(\mathbf{x}_t, t|\mathbf{x}_0)$ and $\hat{\Psi}(\mathbf{x}_t, t|\mathbf{x}_1)$ become accessible. The posterior distribution is then defined by Nelson's duality (Liu et al., 2023b):

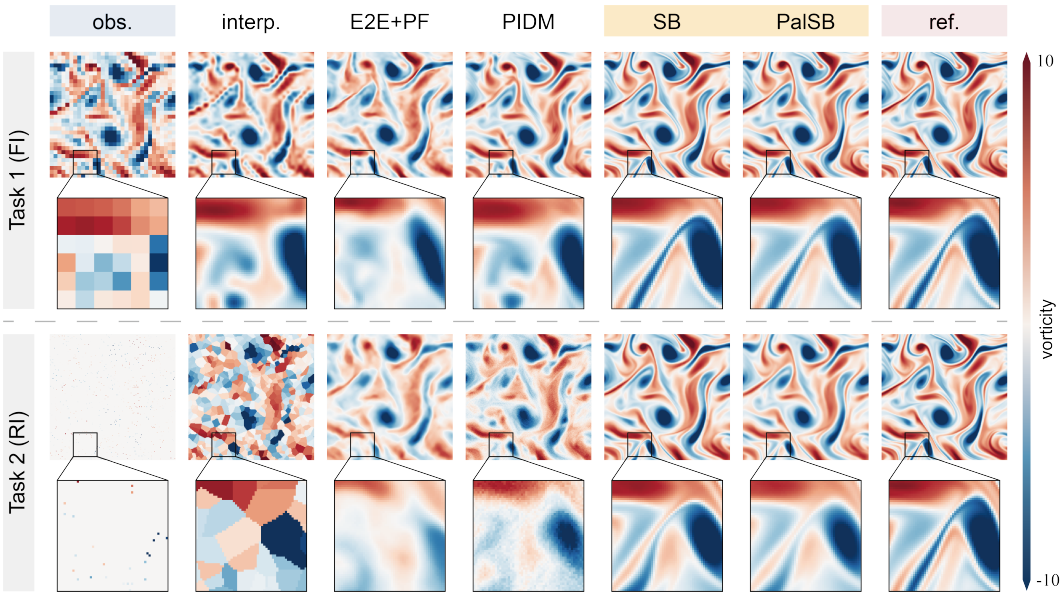

Figure 2: Visual comparison between different methods on the two varying tasks. In the first task (FI, top row), the low-fidelity observation (denoted as obs.) is 8x down-sampled from high-fidelity field of Kolmogorov flow on 256×256 grid. In the second task (RI, bottom row), the observation is randomly sampled from high-fidelity field with 99% of the field masked. Our proposed method (SB and PalSB) visually outperforms other baselines that better recovers the spatial patterns as compared to the reference (denoted as ref.)

$$p_t(\mathbf{x}_t, t|\mathbf{x}_0, \mathbf{x}_1) = \mathcal{N}\left(\mathbf{x}_t; \frac{\bar{\sigma}_t^2}{\bar{\sigma}_t^2 + \sigma_t^2}\mathbf{x}_0 + (1 - \frac{\bar{\sigma}_t^2}{\bar{\sigma}_t^2 + \sigma_t^2})\mathbf{x}_1, \frac{\bar{\sigma}_t^2 \sigma_t^2}{\bar{\sigma}_t^2 + \sigma_t^2}\mathbf{I}\right) \tag{3}$$

where $\sigma_t^2 = \int_0^t \beta(\tau)d\tau$ and $\bar{\sigma}_t^2 = \int_t^1 \beta(\tau)d\tau$ represent the accumulated variances. The DSB model is then trained using paired data $(\mathbf{x}_0, \mathbf{x}_1)$ in a Denoising Diffusion Probabilistic Model (DDPM) style (Ho et al., 2020), with a training objective defined as:

$$\mathcal{J}(\theta) = \|\epsilon_\theta(\mathbf{x}_t, t) - \frac{\mathbf{x}_t - \mathbf{x}_0}{\sigma_t}\| \tag{4}$$

where $\mathbf{x}_t$ is sampled from the analytic posterior distribution in equation 3.

3 Methodology

The pipeline of PalSB, as represented in Fig. 1, includes a two-stage (pretraining and finetuning) training process and a particularly designed sampling process.

3.1 Data-driven pretraining

In the realm of field reconstruction, the boundary distributions for the DSB in Eq. 1 are characterized by the distribution of high-fidelity data, p_0, and the distribution of corrupted data, p_1. The corrupted data samples are derived from high-fidelity samples through the equation:

$$\mathbf{x}_1 = \mathcal{I}(\mathbf{y}) = \mathcal{I}(\mathcal{H}(\mathbf{x}_0) + \epsilon), \quad \mathbf{x}_0 \sim p_0, \quad \epsilon \sim \mathcal{N}(\mathbf{0}, \sigma_\epsilon^2 \mathbf{I}_m) \tag{5}$$

where $\mathcal{I}$ denotes a predefined interpolation function (e.g., nearest, bi-linear, or bi-cubic) that up-scales the sparse observations to match the dimensions of high-fidelity samples.

We find that training directly on high-resolution fields dramatically slows the convergence rate and increases the training time for each iteration. To tackle such problem, inspired by the patch-based training widely used in image restoration (Yang et al., 2019), we train the model on small, randomly cropped local patches from high-resolution field, combined with a scalable network for further inference on global field. This strategy not only focuses on capturing the local structure of the physical field but also mitigates the computational burden associated with processing high-resolution inputs. We then reformulate the training objective to directly parameterize the super-resolving operator, as per the following equation:

$$\mathcal{J}(\theta) = \mathbb{E}_t \mathbb{E}_{\tilde{\mathbf{x}}_0, \tilde{\mathbf{x}}_1 \sim \mathrm{crop}(\mathbf{x}_0, \mathbf{x}_1)} \mathbb{E}_{\mathbf{x}_0, \mathbf{x}_1 \sim p_0, p_1} \left[\| f_\theta(\tilde{\mathbf{x}}_t, \tilde{\mathbf{x}}_1, t) - \tilde{\mathbf{x}}_0 \|^2 \right] \tag{6}$$

Here, f_θ represents the field prediction network, defined as $f_\theta = -\sigma_t \epsilon_\theta + \mathbf{x}_t$. This network is designed to accommodate inputs of varying resolutions, facilitating scalability to higher-resolution inputs (Luo et al., 2023). The pretraining procedure, including this network's deployment, is detailed in Alg. 1, with further implementation specifics discussed in Appendix A.1.

3.2 Physics-aligned Finetuning (PF)

In contrast to conventional image or video generation, the simulation of physical fields needs to take physical laws into consideration, typically expressed as PDEs. These laws are represented by the constraint $\mathcal{F}(\mathbf{x}) = 0$, where $\mathcal{F}$ quantifies deviations from physical laws in a sample.

Due to the spatiotemporal discretization of the generated sample, perfect conformity with these constraints is challenging to achieve. Otherwise, the most straightforward way is to apply physics-informed losses to the one-step prediction $\| \mathcal{F}\left(f_\theta(\tilde{\mathbf{x}}_t, \tilde{\mathbf{x}}_1, t)\right) \|$ as an additional penalty in Eq. 6. However, differing from learning an end-to-end model, the score matching objective in Eq. 6 leads to an expectation (i.e., not a specific sample) over the Gaussian noise on the DSB, which is a single-step rough prediction of the target field. Accordingly, directly optimizing physics-informed loss on such inaccurate predictions hinders the accurate convergence of the training dynamics.

Instead, drawing inspiration from reinforcement learning with human feedback (RLHF) for diffusion models (Lee et al., 2023; Fan et al., 2024), our approach seeks to minimize these deviations on the generated samples throughout the generating path by finetuning the model parameters, θ. The proposed physics-aligned finetuning (PF) objective is formulated as follows:

$$\mathcal{J}_f(\theta) = \mathbb{E}_{\mathbf{y}} \mathbb{E}_{\hat{\mathbf{x}}_0 \sim p_\theta(\mathbf{x}_0|\mathbf{y})} \left[\gamma_{phys} \| \mathcal{F}\left(\hat{\mathbf{x}}_0\right) \| + \gamma_{reg} \| \hat{\mathbf{x}}_0 - \mathbf{x}_0 \| \right] \tag{7}$$

In this equation, $\hat{\mathbf{x}}_0$ represents a sample generated along the sampling path, while γ_{phys} and γ_{reg} are hyperparameters that balance the loss components. Since the ground truth is available, we introduce an additional regression loss (the second term on the right-hand side of equation 7), which acts as a regularization term. This helps maintain the stability of the optimization process and prevents the model from collapsing into a trivial solution, especially when the underlying constraints are ill-posed. This additional term is conceptually similar to the KL-regularization used in DPOK (Fan et al., 2024), which constrains the tuned distribution to remain close to the pretrained distribution. However, in our approach, we directly utilize the pretraining samples $\mathbf{x}_0$, whereas DPOK relies on model-generated samples.

Since the whole objective in Eq. 7 is differentiable w.r.t. the model's parameters, we apply a gradient-based method to directly optimize the finetuning objective. The computational graph of the generating process is unrolled to compute the gradients:

$$\nabla_\theta \mathcal{J}_f(\theta) = \frac{\partial \mathcal{J}_f}{\partial \theta} + \sum_{i=1}^{T} \left(\frac{\partial \mathbf{x}_{t_i}}{\partial \theta} \right)^\top \frac{\partial \mathcal{J}_f}{\partial \mathbf{x}_{t_i}} \tag{8}$$

The indices $0 < t_T < t_{T-1} < ... < t_1 = 1$ represent the diffusion steps used for sample generation, with $\top$ indicating the transpose of the Jacobian matrix. Due to the potentially high memory demand of unrolling the full computational graph, backpropagation is truncated for all steps $i < T$, as suggested in the literature (Prabhudesai et al., 2023; Clark et al., 2023). The specifics of this finetuning process are detailed in Alg. 2 and further discussed in Appendix A.1.

3.3 SAMPLING STRATEGY

Training focused on local features ensures model scalability and data efficiency but may inadvertently neglect the global coherence necessary for physical field reconstructions, particularly with respect to boundary conditions. Moreover, the inherent scalability of neural networks typically restricts them to learning local mappings, necessitating a strategy to integrate global features via the learned local mappings. To address these challenges and enhance the speed of the sampling process, we introduce two simple yet effective techniques:

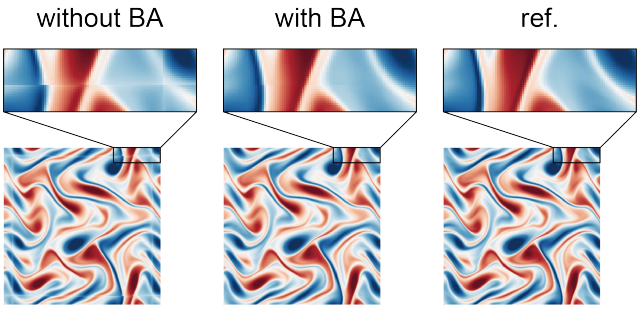

Figure 3: Efficacy of boundary-aware sampling strategy

Boundary-aware sampling (BA). Initially, as illustrated in Figure 4, boundary-aware (BA) sampling begins by padding the low-fidelity input, $\mathbf{y}$, according to the specific type of boundary conditions. Subsequently, the padded input is interpolated to generate the practical input $\mathbf{x}_1$ used during inference: $\mathbf{x}_1 = \mathcal{I}(\text{pad}(\mathbf{y}))$. Notably, this approach is not employed during training because the patch-based training methodology inherently disrupts the original boundary conditions.

Early-stop sampling (ES). As a secondary enhancement, we find that utilizing smaller step sizes combined with an early stop strategy significantly improves performance compared to traditional sampling methods that use larger step sizes for the same NFEs (see Fig. 5). Remarkably, in some instances, even single-step generation achieves performance comparable to the multi-step generation, as demonstrated in Appendix A.1 and Fig. 7.

4 EXPERIMENTAL SETUP

4.1 DATASETS

We choose three different while challenging physical systems to evaluate the capability of the proposed PalSB. A general description of the data are listed as following:

Cylinder flow measured by PIV. Under specific circumstance, the fluid flowing around a blund body (e.g., a cylinder) can induce periodically falling vortices, which is governed by the Navier-Stokes equations quantifying the conservation laws of mass, momentum and energy. The data are gathered from the particle image velocimetry (PIV) experiment, including only a single trajectory of velocity vectors with total length of 879 frames and original resolution of 50×67, in which the former 70% of the trajectory is used for training and the rest is used for test.

2D forced turbulence. Kolmogorov flow (Kolmogorov et al., 1997; Boffetta & Ecke, 2012; Chandler & Kerswell, 2013), a canonical system in studying 2D homogeneous isotropic turbulence (HIT) in fluid dynamics, represents more complicated spatiotemporal patterns controlled by the incompressible Navier-Stokes equations. We use the high-fidelity dataset with spatial resolution of 256×256 published in (Shu et al., 2023), which contains 40 trajectories with 320 frames in each trajectory. We use 90% of the trajectories as the training data and the rest 10% as the test data.

Reaction-diffusion system. Reaction-diffusion system of the Gray-Scott type (simply denoted as RDGS) is another nonliear dynamical system widely tackled in many biological (Maini et al., 2004) and chemical applications (Vervloet et al., 2012). The data used here is simulated on a 256×256 spatial grid with periodic boundary condition. Two trajectories with 3000 frames that start with different initial conditions are used for training and testing, respectively. Notably, with only one trajectory available for training, the amount and diversity of this dataset is much less than the dataset for Kolmogorov flow.

Detailed descriptions of the datasets and the corresponding physical constraints can be found in A.3.

Beyond these 2D cases, PalSB can also work on 3D system. The corresponding description and results can be found in B.1

4.2 Tasks

For each dataset, we train and test the model on two practical tasks in field reconstruction: **(1) Fourier-space interpolation (FI (Buzzicotti, 2023)) and (2) real-space interpolation (RI (Buzzicotti, 2023)).** The former is commonly seen in image-based measurements such as PIV and BOS (Background Oriented Schlieren method), where the physical field cannot be simultaneously acquired at high resolution and covering a large field of view, resulting in a great demand for accurate and data-efficient super-resolution method. On the other hand, the latter usually involves in the intrusive measurements such as hot-wire velocimetry and Pitot, which can interact with the physical field itself, leading to a restricted number of sensor arrangements.

4.3 Baselines

We choose the advanced methods in physical field reconstruction as baselines, including the conventional interpolation method, the End-to-End model based-on FNO (Li et al., 2020) and PIDM (Shu et al., 2023). Detailed description of the baselines can be found in Appendix A.2.

Interpolation. Conventional approach for filling in missing data for field reconstruction from sparse data. In our experiments, bi-cubic interpolation is used for the FI task and nearest interpolation is used for the RI task.

End-to-End model with physics-aligned finetuning. Typical style of supervised learning for data-driven reconstruction of field, directly mapping the low-fidelity data to match with the high-fidelity labels. Here, we choose FNO (Li et al., 2020) as the backbone of the neural network, which is suitable for this task (Takamoto et al., 2022). To make fair comparison, we also apply the physics-informed loss function to finetune the end-to-end model.

PIDM (Shu et al., 2023). With a denoising network pretrained on high-fidelity data as the prior distribution, DDPM can generate the reconstructed field using proper techniques for injecting posterior information such as SDEdit (Meng et al., 2022). In PIDM, by conditioning on the gradient of the equation residual of the input field, the physical insatisfaction of generated contents can be implicitly reduced in some cases.

SB. SB method is the non-finetuned version of PalSB, which is equipped with the same techniques used by PalSB except for the physics-aligned finetuning.

4.4 Evaluation metrics

We use two types of metric that can evaluate the point-wise accuracy and physical insatisfaction, respectively.

nRMSE refers to the normalized relative mean squared error (Raissi et al., 2020), which evaluate the relative L2 error between the reference field and the predicted field. **MSE** refers to the mean squared error (L2 error). **MAE** refers to the mean absolute error (L1 error). **Correlation** refers to the Pearson correlation coefficient. These metrics evaluates the point-wise accuracy of the predicted fields

nER refers to the normalized equation residual (Shu et al., 2023), evaluating the corresponding physical insatisfaction of the given field.

5 Results

5.1 Comparison with Baselines

Figures 2 provides a qualitative comparison between the proposed Physics-aligned Schrödinger Bridge (PalSB) framework and existing baselines, highlighting our framework's superior ability to accurately recover spatial patterns in Kolmogorov flow across two distinct tasks: FI and RI. Additional comparison between the methods is shown in Figs. 12-15

Quantitatively, Table 1 displays the metrics used to evaluate the point-wise accuracy and equation satisfaction of the predicted fields from various models. PalSB shows significant improvements over other state-of-the-art methods across all three physical systems and both tasks. Notably, even when finetuned using the physics-informed loss as in Eq. 7, the E2E model exhibits higher deviations from the physical laws, particularly in systems governed by highly nonlinear equations such as the Kolmogorov flow and the reaction-diffusion system. This can be attributed to challenges in poor initialization of the weights and the tendency of the optimization through a non-convex physics-informed loss to settle into suboptimal local minima, leading to potential convergence failures (Krishnapriyan et al., 2021; Wang et al., 2022a).

Furthermore, the PIDM, while implicitly conditioned on equation residual information, only partially reduces physical dissatisfaction in the Kolmogorov flow and fails in other tests. This underscores the limitations of the DDPM framework in scenarios with insufficient data. The spatiotemporally scattered measurements in the RI task can significantly disrupt the dynamics, as evidenced by the nER metric comparison between FI and RI for the interpolation method in Table 2. This disruption hinders reconstruction through SDEdit that starts from the interpolated field, resulting in poorer performance of PIDM in the RI task.

Moreover, introducing an additional 5% Gaussian noise to the input low-fidelity data only marginally impacts PalSB's performance, demonstrating its robustness in handling noisy observations (detailed descriptions are available in Appendix B.2).

Table 1: Performance comparison of models across different cases and tasks. The metrics with blue color evaluate the errors with the reference data, while the metric with red color evaluates the physics compliance.

Case	Task	Model	nRMSE ↓	MSE ↓	MAE ↓	Correlation ↑	nER ↓
Cy. Flow	FI	Interp.	0.274	2.29E-05	3.06E-03	0.843	5.90E-02
		E2E+PF	0.094	3.42E-06	1.08E-03	0.972	8.32E-03
		PIDM	0.261	2.14E-05	3.05E-03	0.766	1.60E-02
		SB	0.063	**1.36E-06**	7.18E-04	**0.994**	1.50E-02
		PalSB	**0.062**	1.42E-06	**7.04E-04**	0.974	**1.22E-03**
	RI	Interp.	0.301	2.80E-05	3.10E-03	0.898	1.70E+00
		E2E+PF	0.100	3.81E-06	1.17E-03	0.906	9.48E-03
		PIDM	0.121	4.97E-06	1.45E-03	0.894	4.50E-02
		SB	0.092	2.92E-06	1.04E-03	**0.972**	2.10E-02
		PalSB	**0.090**	**2.75E-06**	**1.02E-03**	0.955	**8.74E-04**
Kol. Flow	FI	Interp.	0.538	6.58E-01	1.88E+00	0.857	1.40E-01
		E2E+PF	0.288	1.91E-01	1.04E+00	0.959	3.91E-01
		PIDM	0.512	5.95E-01	1.77E+00	0.871	3.45E-01
		SB	**0.077**	**1.41E-01**	**2.24E-01**	0.996	7.99E-02
		PalSB	0.081	1.56E-01	2.66E-01	**0.997**	**2.40E-02**
	RI	Interp.	0.582	7.69E-01	1.88E+00	0.841	6.22E+02
		E2E+PF	0.466	5.00E-01	1.72E+00	0.908	2.68E+00
		PIDM	0.381	3.31E-01	1.34E+00	0.934	2.73E+01
		SB	**0.230**	**1.23E-01**	**7.16E-01**	**0.973**	1.95E+00
		PalSB	0.253	1.48E+00	8.83E-01	**0.973**	**5.65E-01**
RDGS	FI	Interp.	0.282	2.59E-02	1.01E-01	0.864	3.68E-05
		E2E+PF	0.261	2.18E-02	1.03E-01	0.883	8.17E-05
		PIDM	0.268	2.30E-02	1.06E-01	0.870	1.23E-03
		SB	0.107	4.25E-03	2.66E-02	0.980	1.58E-06
		PalSB	**0.100**	**3.76E-03**	**2.46E-02**	**0.981**	**8.91E-08**
	RI	Interp.	0.292	2.78E-02	9.72E-02	0.855	2.95E-02
		E2E+PF	0.394	3.21E-02	1.25E-01	0.883	5.37E-05
		PIDM	0.277	1.54E-02	9.18E-02	0.918	3.83E-03
		SB	0.194	**1.34E-02**	**5.76E-02**	**0.942**	1.86E-06
		PalSB	**0.193**	1.35E-02	5.79E-02	0.941	**1.69E-07**

5.2 Ablation Studies

Our ablation studies, summarized in Table 2, investigate the effectiveness of specific designed modules within the PalSB framework, with the number of sampling steps fixed at 10. Notably, our

Table 2: Ablation studies across different cases and tasks. The metrics with blue color evaluate the errors with the reference data, while the metric with red color evaluates the physics compliance.

Case	Task	Model	nRMSE ↓	MSE ↓	MAE ↓	Correlation ↑	nER ↓
Cy. Flow	FI	Full model	**0.062**	1.42E-06	**7.04E-04**	0.974	**1.22E-03**
		w/o PF	0.063	**1.36E-06**	7.18E-04	**0.994**	1.54E-02
		w/o DS	**0.062**	1.42E-06	**7.04E-04**	0.974	**1.22E-03**
		w/o ES	0.107	3.72E-06	1.23E-03	0.957	2.68E-03
		w/o BA	-	-	-	-	-
	RI	Full model	**0.090**	**2.75E-06**	**1.02E-03**	0.955	**8.74E-04**
		w/o PF	0.092	2.92E-06	1.04E-03	**0.972**	2.05E-02
		w/o DS	0.092	2.85E-06	1.03E-03	0.944	9.10E-04
		w/o ES	0.129	5.50E-06	1.45E-03	0.921	1.98E-03
		w/o BA	-	-	-	-	-
Kol. Flow	FI	Full model	0.081	1.56E-01	2.66E-01	**0.997**	**2.40E-01**
		w/o PF	**0.077**	**1.41E-01**	**2.24E-01**	**0.997**	7.99E-01
		w/o DS	0.083	1.64E-01	2.72E-01	**0.997**	2.57E-01
		w/o ES	0.340	2.65E+00	1.10E+00	0.950	3.86E-01
		w/o BA	0.109	2.74E-01	3.24E-01	0.994	7.51E-01
	RI	Full model	0.253	1.48E+00	8.83E-01	**0.975**	**5.65E-01**
		w/o PF	**0.230**	**1.23E+00**	**7.16E-01**	**0.975**	1.95E+00
		w/o DS	0.259	1.54E+00	9.02E-01	0.974	6.30E-01
		w/o ES	0.375	3.21E+00	1.33E+00	0.954	9.08E-01
		w/o BA	0.276	1.74E+00	9.51E-01	0.971	1.12E+00
RDGS	FI	Full model	0.100	3.76E-03	**2.46E-02**	**0.981**	**8.91E-08**
		w/o PF	0.107	4.25E-03	2.66E-02	0.980	1.58E-06
		w/o DS	**0.099**	**3.74E-03**	**2.46E-02**	**0.981**	9.51E-08
		w/o ES	0.214	1.52E-02	6.64E-02	0.929	9.00E-07
		w/o BA	0.103	3.98E-03	2.52E-02	0.980	9.31E-08
	RI	Full model	0.193	1.35E-02	5.79E-02	0.941	**1.69E-07**
		w/o PF	0.194	1.34E-02	5.76E-02	0.942	1.86E-06
		w/o DS	0.193	1.33E-02	5.78E-02	0.942	1.90E-07
		w/o ES	**0.184**	**1.19E-02**	**5.62E-02**	**0.946**	7.44E-07
		w/o BA	0.196	1.39E-02	5.91E-02	0.940	**1.69E-07**

physics-aligned finetuning (PF) module significantly reduces the violation of physical laws, even in highly nonlinear and convection-dominant systems, which are typically challenging to optimize from scratch using a PINN-based objective (Krishnapriyan et al., 2021; Wang et al., 2022a). This success is largely due to a data-driven initial point provided by the pretraining stage.

Additionally, several modifications to the sampling process, as shown in Table 2, effectively enhance the final results. These include early-stop (ES), boundary-aware (BA), and deterministic sampling strategies (DS). Specifically, boundary-aware sampling effectively aligns with global effects introduced by boundary conditions, compelling the model to generate content that respects these conditions (see Appendix C.4). Interestingly, removing the Gaussian noise from PalSB's sampling path decreases physical dissatisfaction, and combining this with the early-stop strategy further improves performance. However, removing some modules may slightly enhance point-wise accuracy (nRMSE, MSE, MAE and correlation) while significantly deteriorating performance in terms of nER, indicating a severe breach of physical constraints. Further results and discussions on these ablations are available in Appendix C.

6 Related Work

Data-driven reconstruction of physical field can date from the linear approximation theory such as POD (Berkooz et al., 1993; Everson & Sirovich, 1995; Borée, 2003; Li et al., 2023), Galerkin transforms (Noack & Eckelmann, 1994; Boisson & Dubrulle, 2011) and stochastic estimation (Adrian & Moin, 1988; Suzuki & Hasegawa, 2017), in which the performance on complicated systems are strongly limited by the linear assumption. Based on paired data. further attempts leverage the end-to-end modeling using neural networks, especially, CNN-based networks (Fukami et al., 2019; 2021a;b; Liu et al., 2020; Chai et al., 2020; Ren et al., 2023) and neural operator-based (Li et al.,

2020). Drawing inspirations from computer vision in image super-resolution (Ledig et al., 2017; Wang et al., 2018; 2021), adversarial loss and perceptual loss are introduced for field reconstruction (Yousif et al., 2021; Venkatesh et al., 2021; Li et al., 2023; Güemes et al., 2022). These methods either suffers from poor accuracy on challenging systems (Buzzicotti, 2023) nor struggling with the unstable adversarial training process (Brock et al., 2017; 2019; Miyato et al., 2018; Dhariwal & Nichol, 2021). More importantly, they can misalign with the corresponding physical constraints. Encoding of physical laws into field reconstruction are parially investigated in (Jacobsen et al., 2023; Shu et al., 2023). In particular, instead of directly using PINN loss, PIDM (Shu et al., 2023) inject physical information through CDM in a classifier-free guidance manner. Notably, in many complex nonlinear systems like turbulence, optimizing PINN loss without a good initialization is difficult (Krishnapriyan et al., 2021; Wang et al., 2022a) while implicitly informing the physical information like PI-DDPM can easily make the model ignore this extra input.

The literature related to conditional generation of diffusion models and generation on constrained domain is included in Appendix D

7 Discussion

In this work, we introduce the Physics-aligned Schrödinger Bridge (PalSB) framework, a novel approach for reconstructing physical fields from sparse measurements that effectively addresses the misalignment of physical laws often encountered with diffusion-based models. By employing a patch-based DSB for pretraining, our model achieves a robust initial weight configuration. This setup enhances the stability and efficacy of direct optimization when employing physics-informed losses, thereby preventing divergence. The PalSB framework is further augmented by a meticulously designed sampling process, enabling the accurate reconstruction of physical fields that adhere closely to physical constraints. Our approach is rigorously tested through practical tasks such as FI and RI, where PalSB demonstrates superior performance compared to baseline models across three different physical systems. These systems include challenging environments governed by highly nonlinear PDEs, such as 2D turbulence and reaction-diffusion systems.

The effectiveness of PalSB in these contexts underscores its potential for broad application in generating content that must conform to complex physical constraints within diffusion-based modeling frameworks. The successful implementation of PalSB not only paves the way for more accurate physical field reconstructions but also contributes to the evolving dialogue on integrating physical laws with advanced generative techniques in scientific computing.

8 Limitations

While the PalSB framework effectively aligns generated physical fields with their governing equations, it is important to acknowledge certain limitations. Firstly, the encoding of constraints within PalSB is implemented in a soft manner, implying that some residual discrepancies from the exact equations are inevitable. This soft constraint approach, while facilitating greater flexibility and computational feasibility, does not fully eliminate equation residuals. On the other hand, directly generating complex physical systems, such as those involving turbulence, on the exact solution manifold of the governing equations would be ideal. However, this remains a significant challenge due to the intricate dynamics and high nonlinearity inherent in such systems. Achieving this level of precision and adherence to the governing equations in a generative model is an area of ongoing research and development. Moreover, this study is constrained by computational resources, which has limited our validation to two-dimensional (2D) examples. The extension of our framework to three-dimensional (3D) cases, which are more representative of real-world scenarios, has not yet been tested but is a critical step for future work. This expansion to 3D will enable a more comprehensive assessment of the model's capabilities and applicability across a broader range of scientific and engineering problems.

References

Ronald J. Adrian and Parviz Moin. Stochastic estimation of organized turbulent structure: Homogeneous shear flow. *Journal of Fluid Mechanics*, 190, 1988.

G. Berkooz, P. Holmes, and J. L. Lumley. The Proper Orthogonal Decomposition in the Analysis of Turbulent Flows. *Annual Review of Fluid Mechanics*, 25(Volume 25, 1993), 1993.

Andreas Blattmann, Robin Rombach, Huan Ling, Tim Dockhorn, Seung Wook Kim, Sanja Fidler, and Karsten Kreis. Align Your Latents: High-Resolution Video Synthesis With Latent Diffusion Models. In *Proceedings of the IEEE/CVF Conference on Computer Vision and Pattern Recognition*, 2023.

Guido Boffetta and Robert E. Ecke. Two-Dimensional Turbulence. *Annual Review of Fluid Mechanics*, 44(Volume 44, 2012), 2012.

J. Boisson and B. Dubrulle. Three-dimensional magnetic field reconstruction in the VKS experiment through Galerkin transforms. *New Journal of Physics*, 13(2), 2011.

J. Borée. Extended proper orthogonal decomposition: A tool to analyse correlated events in turbulent flows. *Experiments in Fluids*, 35(2), 2003.

Andrew Brock, Theodore Lim, J. M. Ritchie, and Nick Weston. Neural Photo Editing with Introspective Adversarial Networks. *arXiv:1609.07093*, 2017.

Andrew Brock, Jeff Donahue, and Karen Simonyan. Large Scale GAN Training for High Fidelity Natural Image Synthesis. *arXiv:1809.11096*, 2019.

Charlotte Bunne, Ya-Ping Hsieh, Marco Cuturi, and Andreas Krause. The Schrödinger Bridge between Gaussian Measures has a Closed Form. In *Proceedings of The 26th International Conference on Artificial Intelligence and Statistics*. PMLR, 2023.

Michele Buzzicotti. Data reconstruction for complex flows using AI: Recent progress, obstacles, and perspectives. *Europhysics Letters*, 142(2), 2023.

Salva Rühling Cachay, Bo Zhao, Hailey Joren, and Rose Yu. DYffusion: A Dynamics-informed Diffusion Model for Spatiotemporal Forecasting. *arXiv:2306.01984*, 2023.

Alberto Carrassi, Marc Bocquet, Laurent Bertino, and Geir Evensen. Data assimilation in the geosciences: An overview of methods, issues, and perspectives. *WIREs Climate Change*, 9(5), 2018.

Xintao Chai, Hanming Gu, Feng Li, Hongyou Duan, Xiaobo Hu, and Kai Lin. Deep learning for irregularly and regularly missing data reconstruction. *Scientific Reports*, 10(1), 2020.

Gary J. Chandler and Rich R. Kerswell. Invariant recurrent solutions embedded in a turbulent two-dimensional Kolmogorov flow. *Journal of Fluid Mechanics*, 722, 2013.

Tianrong Chen, Guan-Horng Liu, and Evangelos A Theodorou. Likelihood training of schrödinger bridge using forward-backward sdes theory. In *International Conference on Learning Representations*, 2022.

Yongxin Chen, Tryphon T. Georgiou, and Michele Pavon. On the Relation Between Optimal Transport and Schrödinger Bridges: A Stochastic Control Viewpoint. *Journal of Optimization Theory and Applications*, 169(2), 2016.

Jacob K. Christopher, Stephen Baek, and Ferdinando Fioretto. Projected Generative Diffusion Models for Constraint Satisfaction. *arXiv:2402.03559*, 2024.

Hyungjin Chung, Jeongsol Kim, Michael T. Mccann, Marc L. Klasky, and Jong Chul Ye. Diffusion Posterior Sampling for General Noisy Inverse Problems. *arXiv:2209.14687*, 2023.

Kevin Clark, Paul Vicol, Kevin Swersky, and David J. Fleet. Directly Fine-Tuning Diffusion Models on Differentiable Rewards. *arXiv:2309.17400*, 2023.

Valentin De Bortoli, James Thornton, Jeremy Heng, and Arnaud Doucet. Diffusion Schrödinger Bridge with Applications to Score-Based Generative Modeling. In *Advances in Neural Information Processing Systems*, volume 34. Curran Associates, Inc., 2021.

Prafulla Dhariwal and Alexander Nichol. Diffusion Models Beat GANs on Image Synthesis. In *Advances in Neural Information Processing Systems*, volume 34. Curran Associates, Inc., 2021.

Kieran Didi, Francisco Vargas, Simon V. Mathis, Vincent Dutordoir, Emile Mathieu, Urszula J. Komorowska, and Pietro Lio. A framework for conditional diffusion modelling with applications in motif scaffolding for protein design. *arXiv:2312.09236*, 2024.

R. Everson and L. Sirovich. Karhunen–Loève procedure for gappy data. *Journal of the Optical Society of America A*, 12(8), 1995.

Ying Fan, Olivia Watkins, Yuqing Du, Hao Liu, Moonkyung Ryu, Craig Boutilier, Pieter Abbeel, Mohammad Ghavamzadeh, Kangwook Lee, and Kimin Lee. Reinforcement learning for fine-tuning text-to-image diffusion models. *Advances in Neural Information Processing Systems*, 36, 2024.

Kai Fukami, Koji Fukagata, and Kunihiko Taira. Super-resolution reconstruction of turbulent flows with machine learning. *Journal of Fluid Mechanics*, 870, 2019.

Kai Fukami, Koji Fukagata, and Kunihiko Taira. Machine-learning-based spatio-temporal super resolution reconstruction of turbulent flows. *Journal of Fluid Mechanics*, 909, 2021a.

Kai Fukami, Romit Maulik, Nesar Ramachandra, Koji Fukagata, and Kunihiko Taira. Global field reconstruction from sparse sensors with Voronoi tessellation-assisted deep learning. *Nature Machine Intelligence*, 3(11), 2021b.

Kai Fukami, Koji Fukagata, and Kunihiko Taira. Super-resolution analysis via machine learning: A survey for fluid flows. *Theoretical and Computational Fluid Dynamics*, 37(4), 2023.

Zhihan Gao, Xingjian Shi, Boran Han, Hao Wang, Xiaoyong Jin, Danielle Maddix, Yi Zhu, Mu Li, and Yuyang Wang. PreDiff: Precipitation Nowcasting with Latent Diffusion Models. *arXiv:2307.10422*, 2023.

Alejandro Güemes, Carlos Sanmiguel Vila, and Stefano Discetti. Super-resolution generative adversarial networks of randomly-seeded fields. *Nature Machine Intelligence*, 4(12), 2022.

Jonathan Ho and Tim Salimans. Classifier-Free Diffusion Guidance. *arXiv:2207.12598*, 2022.

Jonathan Ho, Ajay Jain, and Pieter Abbeel. Denoising Diffusion Probabilistic Models. In *Advances in Neural Information Processing Systems*, volume 33. Curran Associates, Inc., 2020.

Jonathan Ho, William Chan, Chitwan Saharia, Jay Whang, Ruiqi Gao, Alexey Gritsenko, Diederik P. Kingma, Ben Poole, Mohammad Norouzi, David J. Fleet, and Tim Salimans. Imagen Video: High Definition Video Generation with Diffusion Models. *arXiv:2210.02303*, 2022a.

Jonathan Ho, Tim Salimans, Alexey Gritsenko, William Chan, Mohammad Norouzi, and David J. Fleet. Video Diffusion Models. *Advances in Neural Information Processing Systems*, 35, 2022b.

Emiel Hoogeboom, Víctor Garcia Satorras, Clément Vignac, and Max Welling. Equivariant Diffusion for Molecule Generation in 3D. In *Proceedings of the 39th International Conference on Machine Learning*. PMLR, 2022.

Emiel Hoogeboom, Jonathan Heek, and Tim Salimans. Simple diffusion: End-to-end diffusion for high resolution images. In *Proceedings of the 40th International Conference on Machine Learning*. PMLR, 2023.

Ilia Igashov, Hannes Stärk, Clément Vignac, Arne Schneuing, Victor Garcia Satorras, Pascal Frossard, Max Welling, Michael Bronstein, and Bruno Correia. Equivariant 3D-conditional diffusion model for molecular linker design. *Nature Machine Intelligence*, 2024.

Christian Jacobsen, Yilin Zhuang, and Karthik Duraisamy. CoCoGen: Physically-Consistent and Conditioned Score-based Generative Models for Forward and Inverse Problems. *arXiv:2312.10527*, 2023.

Andrei Nikolaevich Kolmogorov, V. Levin, Julian Charles Roland Hunt, Owen Martin Phillips, and David Williams. The local structure of turbulence in incompressible viscous fluid for very large Reynolds numbers. *Proceedings of the Royal Society of London. Series A: Mathematical and Physical Sciences*, 434(1890), 1997.

D. Kondrashov and M. Ghil. Spatio-temporal filling of missing points in geophysical data sets. *Nonlinear Processes in Geophysics*, 13(2), 2006.

Aditi Krishnapriyan, Amir Gholami, Shandian Zhe, Robert Kirby, and Michael W Mahoney. Characterizing possible failure modes in physics-informed neural networks. In *Advances in Neural Information Processing Systems*, volume 34. Curran Associates, Inc., 2021.

Christian Ledig, Lucas Theis, Ferenc Huszar, Jose Caballero, Andrew Cunningham, Alejandro Acosta, Andrew Aitken, Alykhan Tejani, Johannes Totz, Zehan Wang, and Wenzhe Shi. Photo-Realistic Single Image Super-Resolution Using a Generative Adversarial Network. In *Proceedings of the IEEE Conference on Computer Vision and Pattern Recognition*, 2017.

Kimin Lee, Hao Liu, Moonkyung Ryu, Olivia Watkins, Yuqing Du, Craig Boutilier, Pieter Abbeel, Mohammad Ghavamzadeh, and Shixiang Shane Gu. Aligning Text-to-Image Models using Human Feedback. *arXiv:2302.12192*, 2023.

Christian Léonard. From the Schrödinger problem to the Monge–Kantorovich problem. *Journal of Functional Analysis*, 262(4), 2012.

Tianyi Li, Michele Buzzicotti, Luca Biferale, Fabio Bonaccorso, Shiyi Chen, and Minping Wan. Multi-scale data reconstruction of turbulent rotating flows with Gappy POD, Extended POD and Generative Adversarial Networks. *Journal of Fluid Mechanics*, 971, 2023.

Zongyi Li, Nikola Borislavov Kovachki, Kamyar Azizzadenesheli, Burigede Liu, Kaushik Bhattacharya, Andrew Stuart, and Anima Anandkumar. Fourier Neural Operator for Parametric Partial Differential Equations. In *International Conference on Learning Representations*, 2020.

Bo Liu, Jiupeng Tang, Haibo Huang, and Xi-Yun Lu. Deep learning methods for super-resolution reconstruction of turbulent flows. *Physics of Fluids*, 32(2), 2020.

Guan-Horng Liu, Tianrong Chen, Evangelos Theodorou, and Molei Tao. Mirror Diffusion Models for Constrained and Watermarked Generation. *Advances in Neural Information Processing Systems*, 36, 2023a.

Guan-Horng Liu, Arash Vahdat, De-An Huang, Evangelos A. Theodorou, Weili Nie, and Anima Anandkumar. I^{2}SB: Image-to-Image Schr\"odinger Bridge. *arXiv:2302.05872*, 2023b.

Aaron Lou and Stefano Ermon. Reflected Diffusion Models. *arXiv:2304.04740*, 2023.

Cheng Lu, Yuhao Zhou, Fan Bao, Jianfei Chen, Chongxuan Li, and Jun Zhu. DPM-Solver++: Fast Solver for Guided Sampling of Diffusion Probabilistic Models. *arXiv:2211.01095*, 2023.

Ziwei Luo, Fredrik K. Gustafsson, Zheng Zhao, Jens Sjölund, and Thomas B. Schön. Image Restoration with Mean-Reverting Stochastic Differential Equations. In *Proceedings of the 40th International Conference on Machine Learning*. PMLR, 2023.

Philip K. Maini, D.L. Sean McElwain, and David I. Leavesley. Traveling Wave Model to Interpret a Wound-Healing Cell Migration Assay for Human Peritoneal Mesothelial Cells. *Tissue Engineering*, 10(3-4), 2004.

Krithika Manohar, Bingni W. Brunton, J. Nathan Kutz, and Steven L. Brunton. Data-Driven Sparse Sensor Placement for Reconstruction: Demonstrating the Benefits of Exploiting Known Patterns. *IEEE Control Systems Magazine*, 38(3), 2018.

Morteza Mardani, Jiaming Song, Jan Kautz, and Arash Vahdat. A Variational Perspective on Solving Inverse Problems with Diffusion Models. *arXiv:2305.04391*, 2023.

Chenlin Meng, Yutong He, Yang Song, Jiaming Song, Jiajun Wu, Jun-Yan Zhu, and Stefano Ermon. SDEdit: Guided Image Synthesis and Editing with Stochastic Differential Equations. *arXiv:2108.01073*, 2022.

Takeru Miyato, Toshiki Kataoka, Masanori Koyama, and Yuichi Yoshida. Spectral Normalization for Generative Adversarial Networks. *arXiv:1802.05957*, 2018.

Bernd R. Noack and Helmut Eckelmann. A global stability analysis of the steady and periodic cylinder wake. *Journal of Fluid Mechanics*, 270, 1994.

Mihir Prabhudesai, Anirudh Goyal, Deepak Pathak, and Katerina Fragkiadaki. Aligning Text-to-Image Diffusion Models with Reward Backpropagation. *arXiv:2310.03739*, 2023.

M. Raissi, P. Perdikaris, and G. E. Karniadakis. Physics-informed neural networks: A deep learning framework for solving forward and inverse problems involving nonlinear partial differential equations. *Journal of Computational Physics*, 378, 2019.

Maziar Raissi, Alireza Yazdani, and George Em Karniadakis. Hidden fluid mechanics: Learning velocity and pressure fields from flow visualizations. *Science*, 367(6481), 2020.

Pu Ren, Chengping Rao, Yang Liu, Zihan Ma, Qi Wang, Jian-Xun Wang, and Hao Sun. PhySR: Physics-informed deep super-resolution for spatiotemporal data. *Journal of Computational Physics*, 492, 2023.

Robin Rombach, Andreas Blattmann, Dominik Lorenz, Patrick Esser, and Björn Ommer. High-Resolution Image Synthesis With Latent Diffusion Models. In *Proceedings of the IEEE/CVF Conference on Computer Vision and Pattern Recognition*, 2022.

Chitwan Saharia, William Chan, Saurabh Saxena, Lala Li, Jay Whang, Emily L. Denton, Kamyar Ghasemipour, Raphael Gontijo Lopes, Burcu Karagol Ayan, Tim Salimans, Jonathan Ho, David J. Fleet, and Mohammad Norouzi. Photorealistic Text-to-Image Diffusion Models with Deep Language Understanding. *Advances in Neural Information Processing Systems*, 35, 2022.

E. Schrödinger. Sur la théorie relativiste de l'électron et l'interprétation de la mécanique quantique. *Annales de l'institut Henri Poincaré*, 2(4), 1932.

Chence Shi, Shitong Luo, Minkai Xu, and Jian Tang. Learning Gradient Fields for Molecular Conformation Generation. In *Proceedings of the 38th International Conference on Machine Learning*. PMLR, 2021.

Dule Shu, Zijie Li, and Amir Barati Farimani. A physics-informed diffusion model for high-fidelity flow field reconstruction. *Journal of Computational Physics*, 478, 2023.

Jiaming Song, Arash Vahdat, Morteza Mardani, and Jan Kautz. Pseudoinverse-Guided Diffusion Models for Inverse Problems. In *International Conference on Learning Representations*, 2022.

Yang Song and Stefano Ermon. Generative Modeling by Estimating Gradients of the Data Distribution. In *Advances in Neural Information Processing Systems*, volume 32. Curran Associates, Inc., 2019.

Yang Song, Jascha Sohl-Dickstein, Diederik P. Kingma, Abhishek Kumar, Stefano Ermon, and Ben Poole. Score-Based Generative Modeling through Stochastic Differential Equations. *arXiv:2011.13456*, 2021.

Xuan Su, Jiaming Song, Chenlin Meng, and Stefano Ermon. Dual Diffusion Implicit Bridges for Image-to-Image Translation. *arXiv:2203.08382*, 2023.

Takao Suzuki and Yosuke Hasegawa. Estimation of turbulent channel flow at based on the wall measurement using a simple sequential approach. *Journal of Fluid Mechanics*, 830, 2017.

Makoto Takamoto, Timothy Praditia, Raphael Leiteritz, Daniel MacKinlay, Francesco Alesiani, Dirk Pflüger, and Mathias Niepert. PDEBench: An Extensive Benchmark for Scientific Machine Learning. *Advances in Neural Information Processing Systems*, 35, 2022.

Zhicong Tang, Tiankai Hang, Shuyang Gu, Dong Chen, and Baining Guo. Simplified diffusion schrödinger bridge. *arXiv:2403.14623*, 2024.

Marivi Tello Alonso, Paco Lopez-Dekker, and Jordi J. Mallorqui. A Novel Strategy for Radar Imaging Based on Compressive Sensing. *IEEE Transactions on Geoscience and Remote Sensing*, 48(12), 2010.

The Event Horizon Telescope Collaboration. First M87 Event Horizon Telescope Results. III. Data Processing and Calibration. *The Astrophysical Journal Letters*, 875(1), 2019.

Alexander Tong, Nikolay Malkin, Kilian Fatras, Lazar Atanackovic, Yanlei Zhang, Guillaume Huguet, Guy Wolf, and Yoshua Bengio. Simulation-free Schrödinger bridges via score and flow matching. *arXiv:2307.03672*, 2024.

Giuseppe Vecchio, Renato Sortino, Simone Palazzo, and Concetto Spampinato. MatFuse: Controllable Material Generation with Diffusion Models. *arXiv:2308.11408*, 2024.

T. S. Sachin Venkatesh, Rajat Srivastava, Pratyush Bhatt, Prince Tyagi, and Raj Kumar Singh. A comparative study of various Deep Learning techniques for spatio-temporal Super-Resolution reconstruction of Forced Isotropic Turbulent flows. In *Volume 10: Fluids Engineering*, 2021.

David Vervloet, Freek Kapteijn, John Nijenhuis, and J. Ruud van Ommen. Fischer–Tropsch reaction–diffusion in a cobalt catalyst particle: Aspects of activity and selectivity for a variable chain growth probability. *Catalysis Science & Technology*, 2(6), 2012.

Sifan Wang, Xinling Yu, and Paris Perdikaris. When and why PINNs fail to train: A neural tangent kernel perspective. *Journal of Computational Physics*, 449, 2022a.

Xintao Wang, Ke Yu, Shixiang Wu, Jinjin Gu, Yihao Liu, Chao Dong, Yu Qiao, and Chen Change Loy. ESRGAN: Enhanced Super-Resolution Generative Adversarial Networks. In *Proceedings of the European Conference on Computer Vision (ECCV) Workshops*, 2018.

Xintao Wang, Liangbin Xie, Chao Dong, and Ying Shan. Real-ESRGAN: Training Real-World Blind Super-Resolution With Pure Synthetic Data. In *Proceedings of the IEEE/CVF International Conference on Computer Vision*, 2021.

Yinhuai Wang, Jiwen Yu, and Jian Zhang. Zero-Shot Image Restoration Using Denoising Diffusion Null-Space Model. *arXiv:2212.00490*, 2022b.

Joseph L. Watson, David Juergens, Nathaniel R. Bennett, Brian L. Trippe, Jason Yim, Helen E. Eisenach, Woody Ahern, Andrew J. Borst, Robert J. Ragotte, Lukas F. Milles, Basile I. M. Wicky, Nikita Hanikel, Samuel J. Pellock, Alexis Courbet, William Sheffler, Jue Wang, Preetham Venkatesh, Isaac Sappington, Susana Vázquez Torres, Anna Lauko, Valentin De Bortoli, Emile Mathieu, Sergey Ovchinnikov, Regina Barzilay, Tommi S. Jaakkola, Frank DiMaio, Minkyung Baek, and David Baker. De novo design of protein structure and function with RFdiffusion. *Nature*, 620(7976), 2023.

Minkai Xu, Lantao Yu, Yang Song, Chence Shi, Stefano Ermon, and Jian Tang. GeoDiff: A Geometric Diffusion Model for Molecular Conformation Generation. *arXiv:2203.02923*, 2022.

Wenming Yang, Xuechen Zhang, Yapeng Tian, Wei Wang, Jing-Hao Xue, and Qingmin Liao. Deep learning for single image super-resolution: A brief review. *IEEE Transactions on Multimedia*, 21 (12):3106–3121, 2019.

Donggeun Yoon, Minseok Seo, Doyi Kim, Yeji Choi, and Donghyeon Cho. Deterministic Guidance Diffusion Model for Probabilistic Weather Forecasting. *arXiv:2312.02819*, 2023.

Mustafa Z. Yousif, Linqi Yu, and Hee-Chang Lim. High-fidelity reconstruction of turbulent flow from spatially limited data using enhanced super-resolution generative adversarial network. *Physics of Fluids*, 33(12), 2021.

Conghan Yue, Zhengwei Peng, Junlong Ma, Shiyan Du, Pengxu Wei, and Dongyu Zhang. Image Restoration Through Generalized Ornstein-Uhlenbeck Bridge. *arXiv:2312.10299*, 2023.

Lvmin Zhang, Anyi Rao, and Maneesh Agrawala. Adding Conditional Control to Text-to-Image Diffusion Models. In *2023 IEEE/CVF International Conference on Computer Vision (ICCV)*, Paris, France, 2023. IEEE. ISBN 9798350307184.

A IMPLEMENTATION DETAILS

A.1 PALSB

The algorithms for pretraining, finetuning and sampling of PalSB are included in Algs. 1, 2 and 3, respectively. The interpolation function $\mathcal{I}(\cdot)$, aiming to interpolate from the input space of $\mathbf{y}$ to the output space of $\mathbf{x}_0$, is chosen to be bi-cubic for FI task while Voronoi tessellation (Fukami et al., 2021b) for RI task.

Compared to training a denoising network that starts from pure noise (such DDPM), the mapping relations for DSB (which start directly from a low-fidelity sample) is easier to learn. Therefore, the scalable neural network used to predict the high-fidelity field can be a simplified U-Net equipped with residual blocks and channel-wise linear attention blocks as suggested in (Luo et al., 2023), removing the group normalization and conventional attention blocks used in DDPM (Ho et al., 2020; Song et al., 2021). The hyperparameters of the network architecture are listed in Table 6.

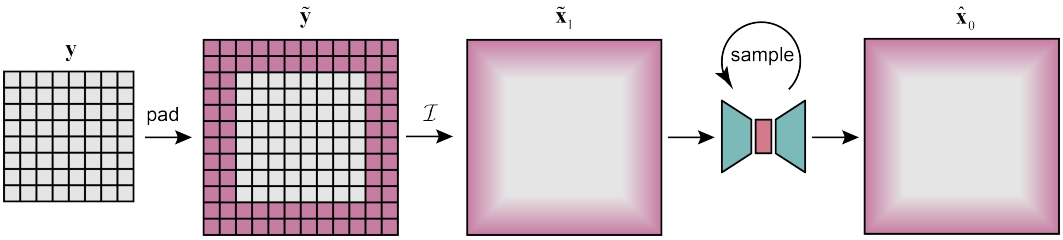

Figure 4: Boundary-aware sampling strategy

The schematic of BA strategy is demonstrated in Fig. 4, where the input low-fidelity data is first padded according to the boundary condition, and then interpolated to match the dimension of high-resolution output. Subsequently, the sampling process is performed on the padded input, after which the padded part of the generated field is trimmed to obtain the final output. Another trick of ES strategy is illustrated in Fig. 5. Under the same NFEs, instead of using a larger step size that covers the full sampling path, we stop the sampling procedure at the early stage with a small step size, regarding the model output from intermediate sample as the final prediction.

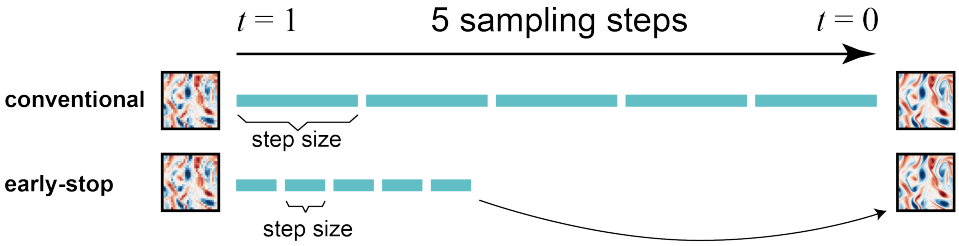

Figure 5: Early-stop sampling strategy

A.2 BASELINES

For the E2E method, we use the FNO (Li et al., 2020), which is a powerful tool for learning the mapping between function space, to fit the direct mapping from low-fidelity field to the high-fidelity one. Notably, the low-fidelity input is also interpolated from the original measurements to keep the same with our method. Since FNO can inherently capture the global interactions within spatial area, we train the model on full fields instead of randomly cropped patches. To make fair comparison, the E2E model is also finetuned using the physics-informed objective as we used for finetuning the PalSB (Eq. 7). The hyperparameters of FNO we used are listed in Table 7.

For the PIDM method, we follow all the settings of in the original paper (Shu et al., 2023) that conditioned on equation residual information. Specifically, we use the pretrained weights for the case of Kolmogorov flow published in (Shu et al., 2023), while training the models for cylinder flow and

Algorithm 1 Pretraining of PalSB

Require: Training dataset $\{\mathbf{x}_0^{(i)}, \mathbf{y}^{(i)}\}_{i=0}^N$, initialized neural network f_θ with parameter group θ, diffusion schedule $\beta(t)$, interpolation function $\mathcal{I}(\cdot)$

while not convergence **do**
  Sample $i \sim U(\{1, 2, ..., N\})$ ▷ Get sample from training dataset
  $\tilde{\mathbf{x}}_0^{(i)}, \tilde{\mathbf{y}}^{(i)} \leftarrow \mathrm{crop}(\mathbf{x}_0^{(i)}), \mathrm{crop}(\mathbf{y}^{(i)})$ ▷ Apply random cropping
  $\tilde{\mathbf{x}}_1^{(i)} \leftarrow \mathcal{I}(\tilde{\mathbf{y}}^{(i)})$ ▷ Interpolate
  Sample $t \sim U(0, 1)$
  $\sigma_t^2 \leftarrow \int_0^t \beta(\tau)d\tau, \bar{\sigma}_t^2 \leftarrow \int_t^1 \beta(\tau)d\tau$
  $C_1 \leftarrow \frac{\bar{\sigma}_t^2}{\bar{\sigma}_t^2 + \sigma_t^2}, C_2 \leftarrow 1 - C_1$
  $\tilde{\mathbf{x}}_t^{(i)} \sim \mathcal{N}\left(C_1\tilde{\mathbf{x}}_0^{(i)} + C_2\tilde{\mathbf{x}}_1^{(i)}, C_1\sigma_t^2\mathbf{I}\right)$
  $\hat{\mathbf{x}}_0^{(i)} \leftarrow f_\theta(\tilde{\mathbf{x}}_t^{(i)}, \tilde{\mathbf{x}}_1^{(i)}, t)$ ▷ Get prediction at step t
  $\mathcal{J}(\theta) \leftarrow \|\hat{\mathbf{x}}_0^{(i)} - \tilde{\mathbf{x}}_0^{(i)}\|$ ▷ Calculate the loss accroding to eq. 6
  Optimize $\mathcal{J}(\theta)$ ▷ Optimize the neural network
end while
$\theta^* \leftarrow \theta$

Algorithm 2 Physics-aligned finetuning of PalSB

Require: Training dataset $\{\mathbf{x}_0^{(i)}, \mathbf{y}^{(i)}\}_{i=0}^N$, initialized neural network f_θ with parameter group θ, pretrained weights θ^*, physical constraints $\mathcal{F}(\cdot)$, diffusion schedule $\beta(t)$, number of sampling steps T, number of backpropogation step B, weights α, β

$\theta \leftarrow \theta^*$ ▷ Start from the pretrained weights
Assign $0 < t_T < t_{T-1} < ... < t_1 = 1$ ▷ Time scheduling
while not convergence **do**
  Sample $\mathbf{x}_0, \mathbf{y} \sim U(\{\mathbf{x}_0^{(i)}, \mathbf{y}^{(i)}\}_{i=0}^N)$ ▷ Get sample from training dataset
  $\mathbf{x}_1 \leftarrow \mathcal{I}(\mathbf{y})$ ▷ Interpolate
  $j \leftarrow 1$
  $\mathbf{x} \leftarrow \mathbf{x}_1$
  while $j < T$ **do** ▷ Sampling loop
    if $j < T - B$ **then**
      $\mathbf{x} \leftarrow \mathrm{sg}(\mathbf{x})$ ▷ Truncate the gradient to save memory
    end if
    $\hat{\mathbf{x}}_0 \leftarrow f_\theta(\mathbf{x}, \mathbf{x}_1, t_j)$
    $\sigma_{t_j}^2 \leftarrow \int_0^{t_j} \beta(\tau)d\tau; \bar{\sigma}_{t_j}^2 \leftarrow \int_{t_j}^1 \beta(\tau)d\tau$
    $C_1 \leftarrow \frac{\bar{\sigma}_{t_j}^2}{\bar{\sigma}_{t_j}^2 + \sigma_{t_j}^2}; C_2 \leftarrow 1 - C_1$
    $\mathbf{x} \sim \mathcal{N}\left(C_1\hat{\mathbf{x}}_0 + C_2\mathbf{x}_1, C_1\sigma_{t_j}^2\mathbf{I}\right)$
    $j \leftarrow j + 1$
  end while
  $\mathcal{J}(\theta) \leftarrow \alpha\|\hat{\mathbf{x}}_0 - \mathbf{x}_0\| + \beta\|\mathcal{F}(\hat{\mathbf{x}}_0)\|$ ▷ Calculate the loss according to eq. 7
  Optimize $\mathcal{J}(\theta)$
end while

Algorithm 3 Sampling process of PalSB

Require: Measurements $\mathbf{y}$, trained neural network f_θ, diffusion schedule $\beta(t)$, number of sampling steps T, boundary padding function $\mathrm{pad}(\cdot)$ and the corresponding boundary trimming function $\mathrm{trim}(\cdot)$

Assign $0 < t_T < t_{T-1} < ... < t_1 = 1$ ▷ Time scheduling
$\mathbf{y} \leftarrow \mathrm{pad}(\mathbf{y})$ ▷ Pad the field according to the boundary condition
$\mathbf{x}_1 \leftarrow \mathcal{I}(\mathbf{y})$ ▷ Interpolate
$\mathbf{x} \leftarrow \mathbf{x}_1$
$j \leftarrow 1$
while $j < T$ **do** ▷ Sampling loop with early-stop strategy
    $\hat{\mathbf{x}}_0 \leftarrow f_\theta(\mathbf{x}, \mathbf{x}_1, t_j)$
    $\sigma^2_{t_j} \leftarrow \int_0^{t_j} \beta(\tau)d\tau; \bar{\sigma}^2_{t_j} \leftarrow \int_{t_j}^1 \beta(\tau)d\tau$
    $C_1 \leftarrow \frac{\bar{\sigma}^2_{t_j}}{\bar{\sigma}^2_{t_j} + \sigma^2_{t_j}}; C_2 \leftarrow 1 - C_1$
    $\mathbf{x} \leftarrow C_1\hat{\mathbf{x}}_0 + C_2\mathbf{x}_1$ ▷ Deterministic sampling path
    $j \leftarrow j + 1$
end while
$\hat{\mathbf{x}}_0 \leftarrow \mathrm{trim}(\hat{\mathbf{x}}_0)$ ▷ Trim the padded boundary grids

reaction-diffusion system from scratch. Note that the DDPM-based method which start from pure Gaussian noise cannot easily scale up to larger domain (Hoogeboom et al., 2023). Therefore, we also train the PIDM on full fields instead of randomly cropped patches. All the neural networks for PIDM share the same architecture, where the hyperparameters are listed in the original paper. Based on SDEdit and classifier-free guidance, the sampling process of PIDM in our experiments follows the original paper that uses the same parameters as suggested in its Github repository (Shu et al., 2023).

A.3 Datasets description

Cylinder flow measured by PIV. Due to the limitation of PIV experiment, the pressure field is not accessible, which means the governing equations cannot be fully characterized as physical constraints. Here, we only consider the constraints of continuity (which refer to the mass conservatin of the fluid) as following

$$\nabla \cdot \mathbf{u} = 0 \tag{9}$$

where $\nabla\cdot$ is the divergence operator and $\mathbf{u}$ is the 2D velocity vector field.

2D forced turbulence. The Kolmogorov flow follows the vorticity equation derived from Navier-Stokes equations written as

$$\frac{\partial \omega}{\partial t} + \mathbf{u} \cdot \nabla \omega - \frac{1}{Re}\nabla^2 \omega = \mathbf{f} \tag{10}$$

where $\mathbf{u} \equiv [u, v]$ is the velocity vector field, $\omega \equiv \partial v/\partial x - \partial u/\partial y$ is the vorticity field, Reynolds number Re is a constant scalar and $\mathbf{f}$ is the external force defined in (Shu et al., 2023). Assuming the periodic boundary condition, the velocity in this equation can be easily determined by solving a Poisson equation in Fourier space. Therefore, the equation residual can be calculated given a sample of vorticity field.

Reaction-diffusion system. The governing equation of RDGS is written as

$$\begin{aligned} \frac{\partial u}{\partial t} &= \mu_u \Delta u - uv^2 + F(1-u) \\ \frac{\partial v}{\partial t} &= \mu_v \Delta v + uv^2 - (F+\kappa)v \end{aligned} \tag{11}$$

where u and v are the concentration variables, μ_u and μ_v are the diffusion coefficients, F and κ are the parameters that control the reaction source terms, and Δ denotes the Laplacian operator. We use finite difference method to calculate the derivatives in the equations.

A.4 Runtime environment

All the experiments conducted in this paper are running on a single GPU of Nvidia GeForce RTX 3090 with Intel(R) Xeon(R) Gold 6226R CPU. The platform is Ubuntu 20.04.3 LTS operation system with Python 3.9 environment. We list the parameters for reproducing our experiments in Tables 8 and 9, including the training, finetuning and sampling process.

B Further results

Table 3: Performance comparison of models on NS3D FI and NS3D RI cases with noise-free and noisy data.

Case	Model	nRMSE ↓	MSE ↓	L1 Error ↓	Correlation ↑	nER ↓
NS3D FI (noise-free)	PalSB	**0.0928**	**0.0043**	**0.0457**	**0.9954**	**3.8502**
	interp.	0.3263	0.0539	0.1663	0.9415	14.0915
NS3D FI (5% noise)	PalSB	**0.0948**	**0.0045**	**0.0468**	**0.9953**	**3.8700**
	interp.	0.3267	0.0540	0.1665	0.9414	14.2528
NS3D RI (noise-free)	PalSB	**0.1846**	**0.0168**	**0.0929**	**0.9820**	**2.4647**
	interp.	0.3645	0.0669	0.1758	0.9299	625.9368
NS3D RI (5% noise)	PalSB	**0.1850**	**0.0168**	**0.0931**	**0.9820**	**2.4701**
	interp.	0.3654	0.0672	0.1766	0.9296	629.2205

B.1 Extension on 3D dataset

To validate the capability of our methodology beyond 2D cases, we further test the PalSB on a complex 3D system for both FI and RI tasks. The 3D dynamical system is describe by the compressible Navier-Stokes equations, which contains the following continuity equation and momentum equation

$$\begin{aligned} \partial_t \rho + \nabla \cdot (\rho \mathbf{v}) &= 0 \\ \rho \left(\partial_t \mathbf{v} + \mathbf{v} \cdot \nabla \mathbf{v}\right) &= -\nabla p + \eta \Delta \mathbf{v} + (\zeta + \eta/3) \nabla (\nabla \cdot \mathbf{v}) \end{aligned} \tag{12}$$

where $\mathbf{v}$ is the 3D velocity vector, ρ is the density, p is the pressure, and ζ and η are bulk and shear viscosity, respectively. while challenging due to the highly nonlinear nature of the governing equations, this problem is significant in many applications like aerodynamics.

The training and testing dataset is drawn from PDEBench Takamoto et al. (2022) with $\eta = \zeta = 1e-8$, periodic boudaries and turbulent initial conditions, which contains 600 trajectories of $\mathbf{v}$, ρ and p. Each trajectory contains 21 snapshots spatially discretized on a $64 \times 64 \times 64$ grid. We train our model on the first 90% of the trajectories and test on the rest. We perform 4x super-resolution for FI task and 1% observation reconstruction for RI task. As illustrated in Figs. 20,21 and Table 3, PalSB can still make accurate predictions in 3D configurations, representing the power of PalSB in modeling a wide range of physical systems.

B.2 Noisy observations

In order to assess the robustness of the models, we add Gaussian noise with 5% of the standard deviation of the corresponding data into the input low-fidelity field. As shown in Table 4, PalSB maintains similar performance as in noise-free cases. Particularly, in the two tasks of reaction-diffusion system where there is large area that is not diffused, PalSB recovers these areas even perturbed with noise (Fig. 18 and 19).

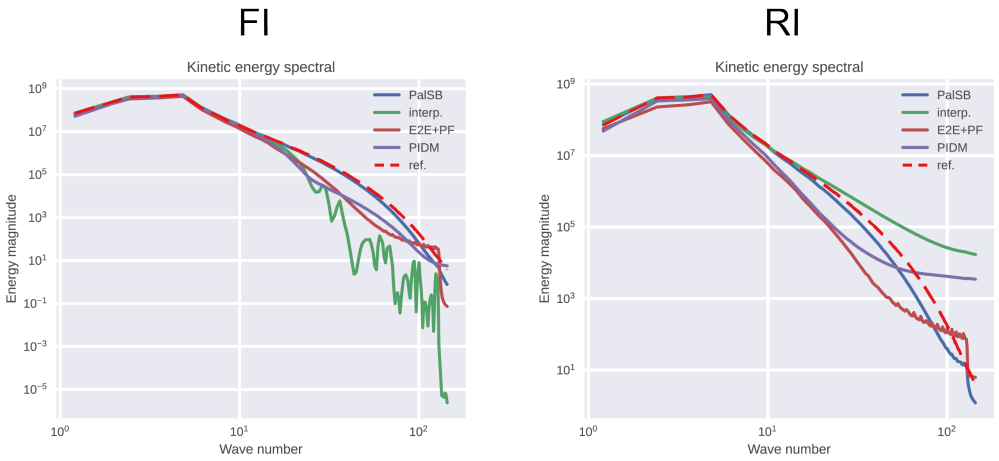

Figure 6: Statistical comparison of the methods on Kolmogorov flow.

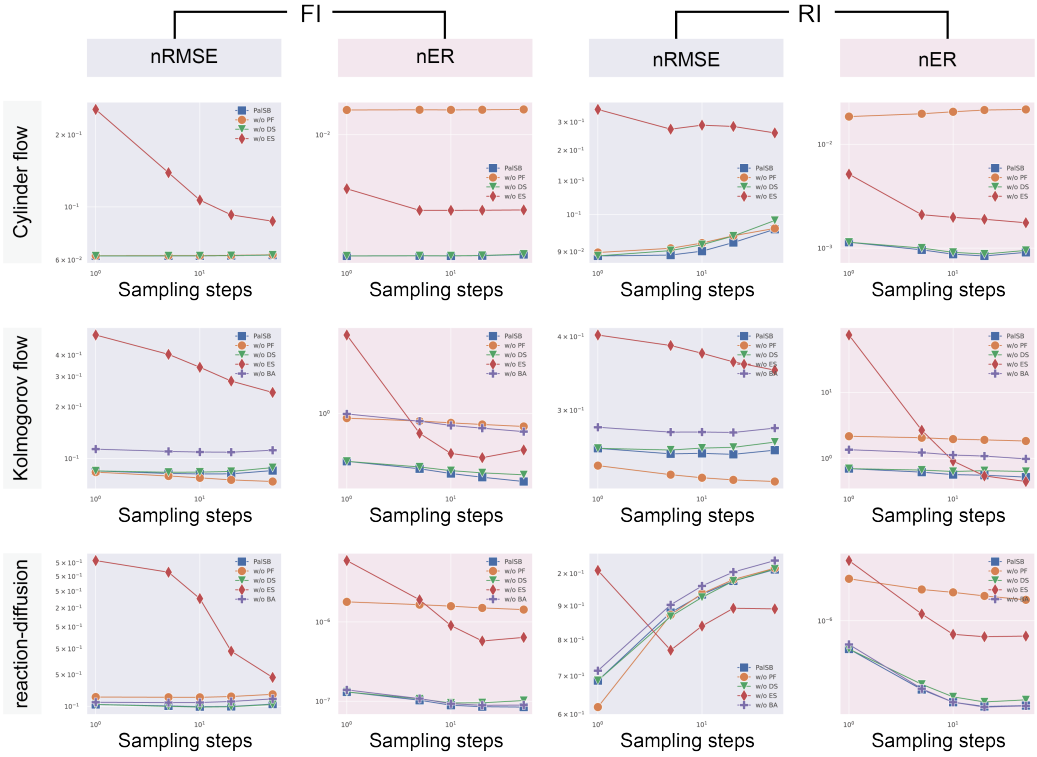

Figure 7: Ablations on sampling steps.

B.3 Statistics of the Kolmogorov flow

Kinetic energy spectral (KES) of the turbulent flow (Boffetta & Ecke, 2012), vital statistics of the energy distribution on varying spatial frequency components, is calculated for the fields predicted by different methods as shown in Fig. 6, where the red dot-line represents the KES from the high-fidelity simulation data. In both tasks, the turbulent fields generated by PalSB can better capture the kinetic energy distribution in spectral space than other methods, indicating the efficacy of PalSB in remembering the data statistics.

C ABLATIONS

C.1 NUMBER OF SAMPLING STEPS

As shown in Figs. 7 and 11, though the increase of sampling steps does not necessarily facilitate the accuracy and physical satisfaction, in most cases, more sampling steps can reduce the nER. These phenomena can be first attributed to the restricted sampling steps for finetuning that the model gets overfitted around the configured number of sampling steps. Besides, as investigated in diffusion-based image restoration studies (Luo et al., 2023), the multi-step generation through the diffusion path represent particular capability in generating contents that look like the samples in training dataset, which, in other word, can keep statistical consistency with the target distribution of the dataset while may diverge on the point-wise accuracy. Consequently, we choose 10 steps to sample the field that makes a proper trade-off between performance and time consumption.

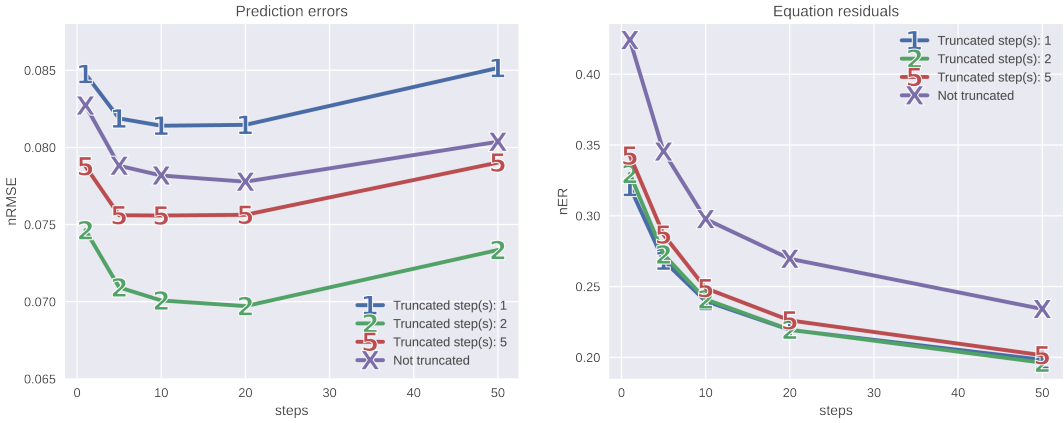

Figure 8: Ablations on the number of truncated steps in finetuning, which is tested on FI task for Kolmogorov flow.

C.2 NUMBER OF TRUNCATED STEPS IN FINETUNING

In the finetuning stage, the backpropagation along the sampling path is truncated to save the computational consumption. The number of truncated steps in finetuning (i.e., B in Alg. 2) can affect the performance of PalSB as seen in Fig. 8. In addition to the higher computational costs, we find that a larger number of backpropagation steps does not necessarily enhance the results. Excessive steps of backpropagation might lead to difficulty for the model's convergence to the global optimum within a given number of iterations.

C.3 DIFFUSION SCHRÖDINGER BRIDGE

Based on the observation mentioned above that he increase of sampling steps does not necessarily facilitate the accuracy of the model prediction, we further train the same neural network without using diffusion path, which is, in fact, an E2E model that directly optimizes the regression loss. As demonstrated in Table 5, we find that even such model can achieve a higher accuracy than the model trained by diffusion-like loss, it is still not convincing in characterizing the statistical features of physical field and shows higher violation against the physics. Moreover, such deterministic model is unable to evaluate the uncertainty.

C.4 BOUNDARY-AWARE SAMPLING

Considering that the scalability of the neural network used for PalSB results in obstacles for capturing global patterns that introduced by boundary conditions, this strategy is critical for PalSB to enforce the boundary conditions as illustrated in Fig. 3. Here, the periodic boundary condition is well aligned through the sampling on the padded field, which enforce the model to be aware of the global information in a local manner. As shown in Fig. 3, padding is applied to the low-fidelity observation

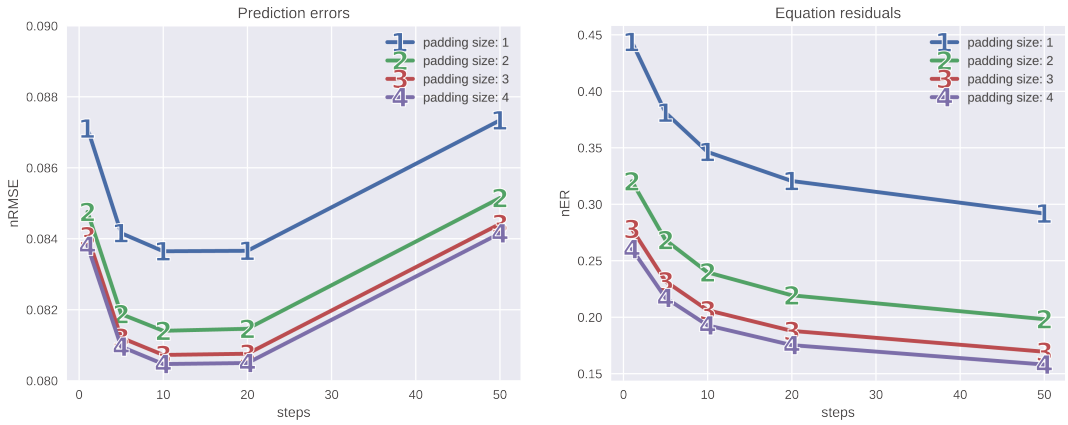

Figure 9: Ablations on the size of padding in sampling, which is tested on FI task for Kolmogorov flow.

y before interpolation to the original grid. Consequently, the choice of padding size for FI and RI tasks depends on the size of the observation. Specifically, the padding size along each direction is set to 2 for the FI task and 16 for the RI task, respectively. This ensures consistency in the size of the interpolated data samples in each case.

We further examine the impact of padding size on the final performance in the Kolmogorov flow case. As illustrated in Fig. 9, increasing the padding size improves the final performance. However, this improvement comes with additional computational costs, as the neural network must process a larger input. Therefore, a trade-off between performance and computational cost should be carefully considered when employing boundary-aware sampling.

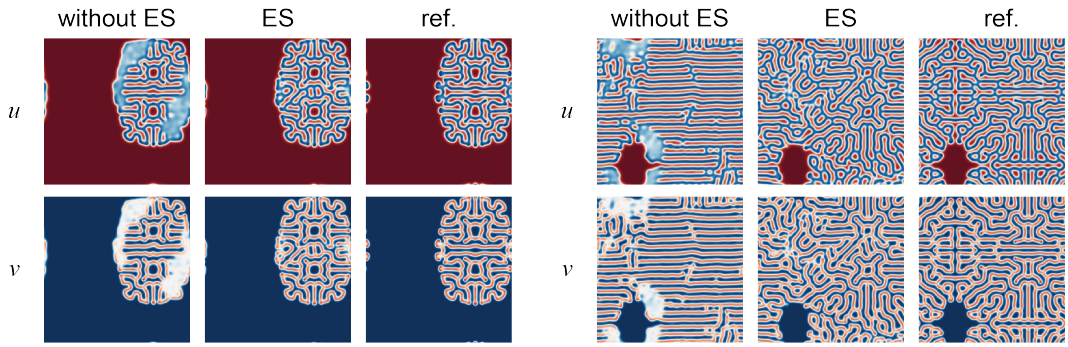

Figure 10: Ablations on early-stop sampling strategy. This reaction-diffusion case on RI task indicates that a lower nRMSE do not mean physically reasonable.

C.5 Early-stop sampling strategy

Under the same number of function evaluation (NFE), we find that sampling with a small time step and then stopping at the early stage is a better strategy than increasing the step size as implemented in existing work (Fig. 7 and Fig. 11). Smaller step size can possibly reduce the discretization error for the first few steps on sampling path to more accurately simulate the sample from the posterior distribution at intermediate step, yielding significant improvements in most experiments when the NFEs are relatively low (e.g., less than 50 NFEs). Although the nRMSE on reaction-diffusion system shows that the model without early-stop sampling is better, we find its failure in generated spatial patterns as illustrated in Fig. 10, indicating the bias for only using the point-wise accuracy as the evaluation metric.

C.6 DETERMINISTIC SAMPLING

Removing all the Gaussian noise in sampling path leads to a deterministic sampling process that is the same as OT-ODE in (Liu et al., 2023b). To our surprise, such procedure shows enhancement on nER in our experiments, even the model is not trained with deterministic DSB (i.e., not trained with OT-ODE). We suppose that this phenomenon is related to the symmetric noise schedule of DSB, which is nearly noise-free at the two ends of the sampling path, making it possible for the neural network to generalize to noise-free input at the early stage of the sampling process.

Table 4: Performance comparison of models across different cases and tasks on noisy observations (5% Gaussian noise). The metrics with blue color evaluate the errors with the reference data, while the metric with red color evaluates the physics compliance.

Case	Task	Model	nRMSE ↓	MSE ↓	MAE ↓	Correlation ↑	nER ↓
Cy. Flow	FI	Interp.	0.276	2.33E-05	3.13E-03	0.842	6.64E-02
		E2E+PF	0.094	3.42E-06	1.09E-03	0.972	8.35E-03
		PIDM	0.262	2.14E-05	3.05E-03	0.768	1.59E-02
		SB	**0.063**	**1.37E-06**	7.22E-04	**0.994**	1.54E-02
		PalSB	**0.063**	1.43E-06	**7.10E-04**	0.975	**1.23E-03**
	RI	Interp.	0.303	2.85E-05	3.19E-03	0.890	1.73E+00
		E2E+PF	0.100	3.82E-06	1.17E-03	0.909	9.59E-03
		PIDM	0.121	4.98E-06	1.45E-03	0.899	4.59E-02
		SB	0.093	2.95E-06	1.05E-03	**0.971**	2.04E-02
		PalSB	**0.091**	**2.79E-06**	**1.03E-03**	0.953	**8.83E-04**
Kol. Flow	FI	Interp.	0.540	6.62E-01	1.88E+00	0.856	1.52E-01
		E2E+PF	0.288	1.92E-01	1.04E+00	0.959	3.93E-01
		PIDM	0.524	6.23E-01	1.83E+00	0.859	3.84E-01
		SB	**0.085**	**1.68E-01**	**2.61E-01**	**0.996**	8.54E-02
		PalSB	0.088	1.79E-01	2.91E-01	**0.996**	**2.72E-02**
	RI	Interp.	0.584	7.75E-01	1.86E+00	0.840	6.27E+02
		E2E+PF	0.466	5.00E-01	1.72E+00	0.908	2.70E+00
		PIDM	0.382	3.33E-01	1.34E+00	0.934	2.79E+01
		SB	**0.233**	**1.26E-01**	**7.33E-01**	**0.972**	1.98E+00
		PalSB	0.255	1.50E+00	8.90E-01	**0.972**	**5.73E-01**
RDGS	FI	Interp.	0.284	2.61E-02	1.06E-01	0.861	4.63E-04
		E2E+PF	0.261	2.18E-02	1.03E-01	0.883	8.18E-05
		PIDM	0.268	2.31E-02	1.06E-01	0.870	1.30E-03
		SB	0.107	4.27E-03	2.67E-02	0.980	1.59E-06
		PalSB	**0.100**	**3.77E-03**	**2.47E-02**	**0.981**	**9.13E-08**
	RI	Interp.	0.294	2.81E-02	1.04E-01	0.851	3.02E-02
		E2E+PF	0.394	5.02E-02	1.63E-01	0.701	5.39E-05
		PIDM	0.217	1.55E-02	9.20E-02	0.918	3.92E-03
		SB	**0.194**	**1.34E-02**	**5.78E-02**	**0.941**	1.87E-06
		PalSB	**0.194**	1.35E-02	5.81E-02	0.939	**1.74E-07**

D FURTHER DISCUSSION ON RELATED WORK

D.1 CONDITIONAL GENERATION WITH DIFFUSION MODELS

Diffusion models (Song & Ermon, 2019; Ho et al., 2020; Song et al., 2021) are widely applied to the generation of diverse contents, especially image (Dhariwal & Nichol, 2021; Rombach et al., 2022; Saharia et al., 2022), video (Ho et al., 2022b;a; Blattmann et al., 2023) and molecular (Xu et al., 2022; Watson et al., 2023; Igashov et al., 2024). Particularly, conditional generation using diffusion model based on given information is highly regarded in practical scenes such as image/video restoration (Dhariwal & Nichol, 2021; Ho & Salimans, 2022; Meng et al., 2022; Song et al., 2022; Mardani et al., 2023; Chung et al., 2023; Song et al., 2021; Wang et al., 2022b; Yue et al., 2023; Luo et al., 2023; Zhang et al., 2023; Liu et al., 2023b), molecular generation (Shi et al., 2021; Xu et al., 2022; Watson et al., 2023; Igashov et al., 2024; Vecchio et al., 2024; Didi et al., 2024) and dynamic forecasting (Gao et al., 2023; Yoon et al., 2023; Cachay et al., 2023), basically categorized into two classes that based on unconditional diffusion model (UDM) and conditional diffusion model

Table 5: Ablation on DSB training

Case	Task	Model	nRMSE ↓	MSE ↓	MAE ↓	Correlation ↑	nER ↓
Cy. Flow	FI	w/o DSB	0.063	1.41E-06	7.18E-04	0.973	1.38E-03
		w/ DSB (10 steps)	0.062	1.42E-06	7.04E-04	0.974	1.22E-03
	RI	w/o DSB	0.081	2.35E-06	8.98E-04	0.967	1.44E-03
		w/ DSB (10 steps)	0.090	2.75E-06	1.02E-03	0.955	8.74E-04
Kol. Flow	FI	w/o DSB	0.075	1.34E-01	2.30E-01	0.998	3.34E-01
		w/ DSB (10 steps)	0.081	1.56E-01	2.66E-01	0.997	2.40E-01
	RI	w/o DSB	0.223	1.14E+00	7.98E-01	0.983	1.01E+00
		w/ DSB (10 steps)	0.253	1.48E+00	8.83E-01	0.975	5.65E-01
RDGS	FI	w/o DSB	0.092	3.23E-03	2.21E-02	0.984	6.38E-08
		w/ DSB (10 steps)	0.100	3.76E-03	2.46E-02	0.981	8.91E-08
	RI	w/o DSB	0.140	6.86E-03	4.18E-02	0.967	1.06E-06
		w/ DSB (10 steps)	0.193	1.35E-02	5.79E-02	0.941	1.69E-07

(CDM) respectively. Utilizing a pretrained UDM as *a priori* distribution, methods such as (Ho & Salimans, 2022; Chung et al., 2023; Song et al., 2022; Wang et al., 2022b; Mardani et al., 2023) manipulate the generating path towards the required condition, which is usually performed through the gradient-based correction. By partially noising the conditions along the forward diffusion path and then running the reversed process, SDEdit (Meng et al., 2022) can approximately sample from the target conditional distribution. ControlNet is another popular tool appended to a pretrained UDM, injecting conditional information through finetuning an additional feature adjusting network on paired data. Classifier-free guidance (Ho & Salimans, 2022) uses a weighted combination of UDM and CDM to guide the sampling path. Instead of training a UDM that requires intensive data and computational resources, CDM directly add the conditional information as an additional input of the model. As a special case of CDM, instead of starting from Gaussian noise, DSB (De Bortoli et al., 2021; Bunne et al., 2023; Liu et al., 2023b; Tong et al., 2024; Yue et al., 2023) directly learns the probabilistic path from the conditions to the targets, which is much more fast-to-train and data-efficient for specific task. Despite the empirically proved efficacy on image/audio tasks, the modeling of physical field using DSB is not well studied, which is addressed in this work.

D.2 Generation on constrained domain

Diffusion model is adept to characterize the statistics of training data yet does not guarantee the satisfaction of constraints for the generated contents. There are efforts to apply simple constraints on diffusion models. Specifically, pixel-wise thresholding during generation (Ho et al., 2020; Saharia et al., 2022; Lu et al., 2023) is a simple while effective trick to fulfill the value range of an image. Similarly, mirror diffusion model (Liu et al., 2023a; Lou & Ermon, 2023) leverages the mirror mapping to restrict the generation not exceeding a given convex set. Generation with equaivariance (Hoogeboom et al., 2022; Igashov et al., 2024) is another class of methods that are ubiqitous in molecular related problems. Projected generative diffusion model (Christopher et al., 2024) further extended the constraints to more complicated domain on the support of ΠGDM (Song et al., 2022). However, these methods can only work on tractable domain of constraints, failing when the sample is embedded on a complicated and intractable manifold such as the physical field that derived from the solution of highly nonlinear PDEs.

E Code and data availability

The code for PalSB is submitted as the supplementary material. The data and trained checkpoints can be downloaded at the Google Drive after the paper's acceptance.

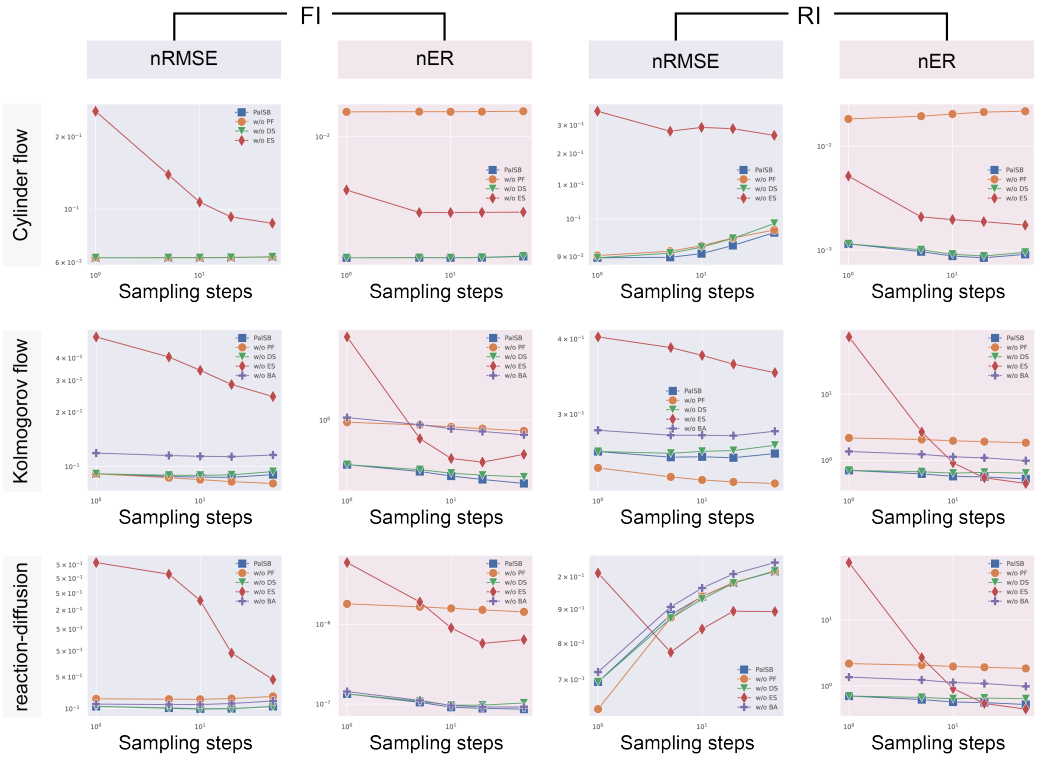

Figure 11: Ablations on sampling steps (5% noise).

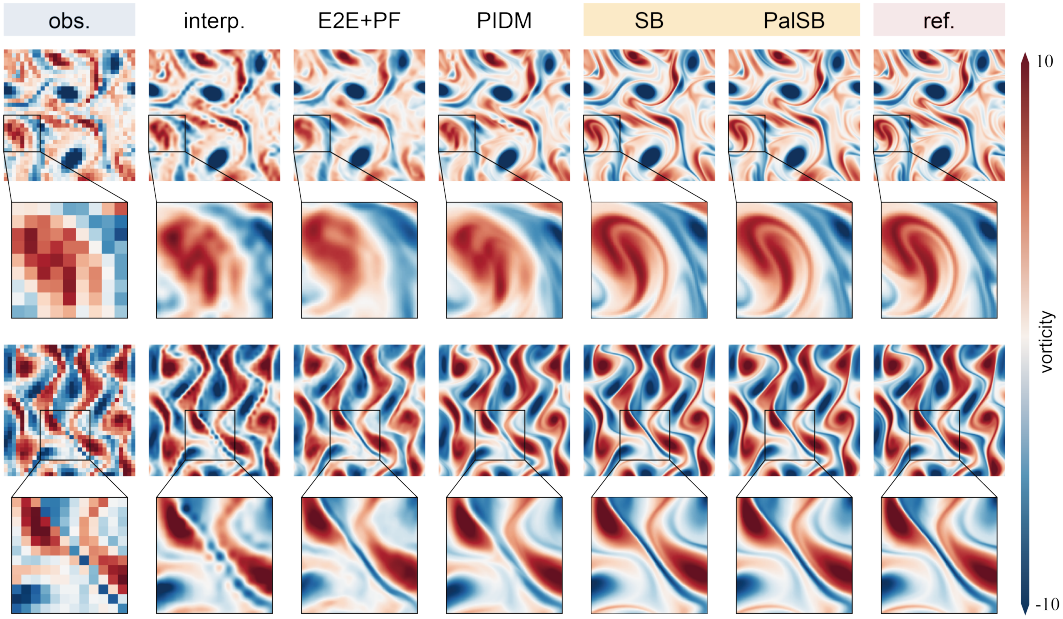

Figure 12: Additional results of Kolmogorov flow on FI task (8x super-resolution, noise-free).

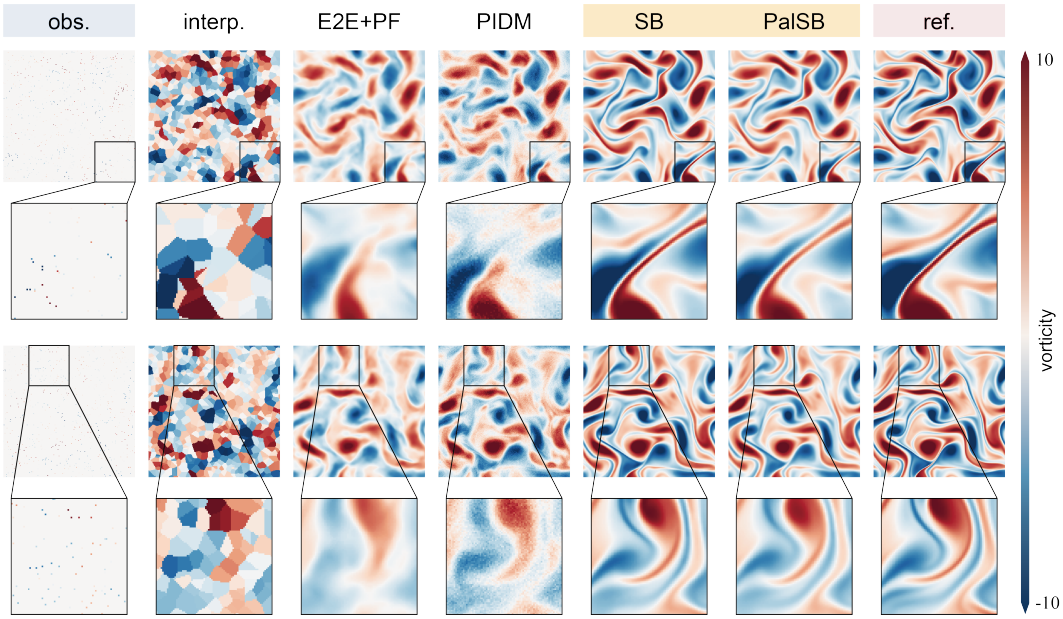

Figure 13: Additional results of Kolmogorov flow on RI task (99% masked, noise-free).

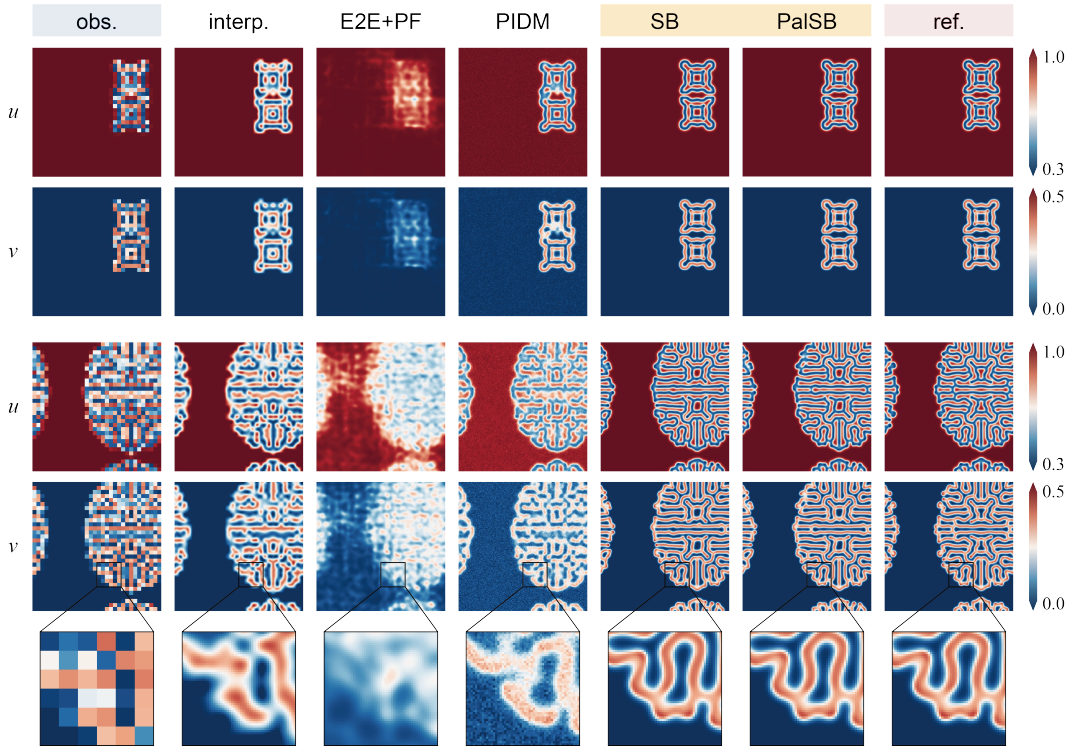

Figure 14: Additional results of GS-RD on FI task using noise-free observations (8x super-resolution, 0% Gaussian noise).

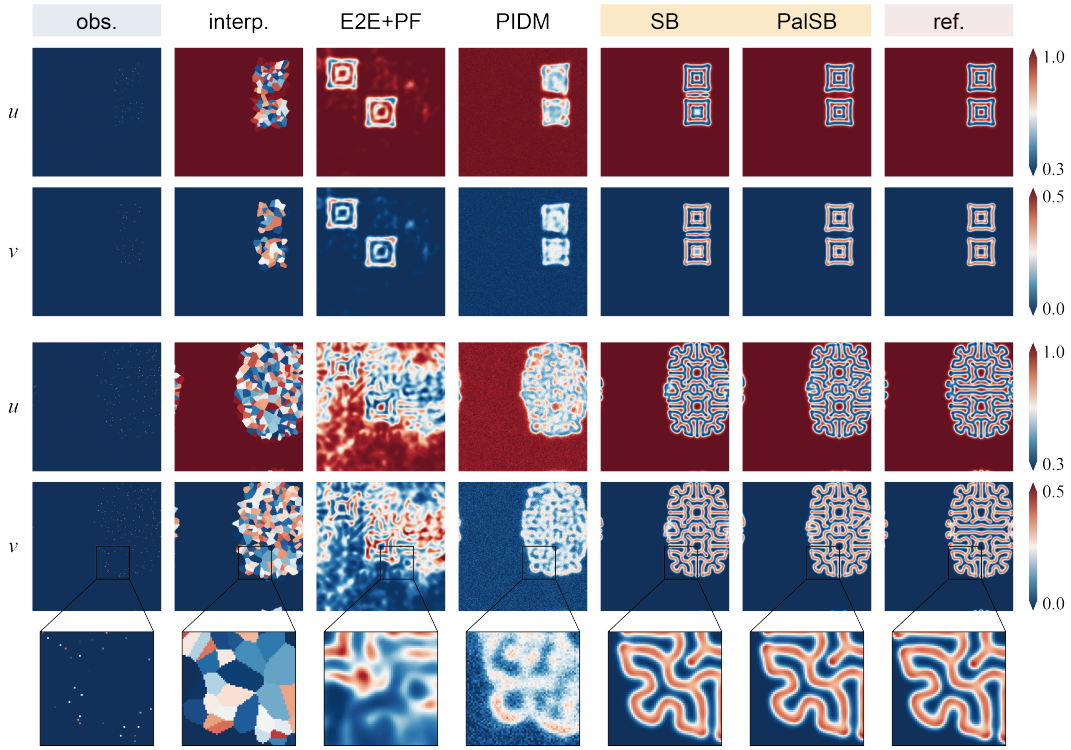

Figure 15: Additional results of GS-RD on RI task using noise-free observations (99% masked, noise-free).

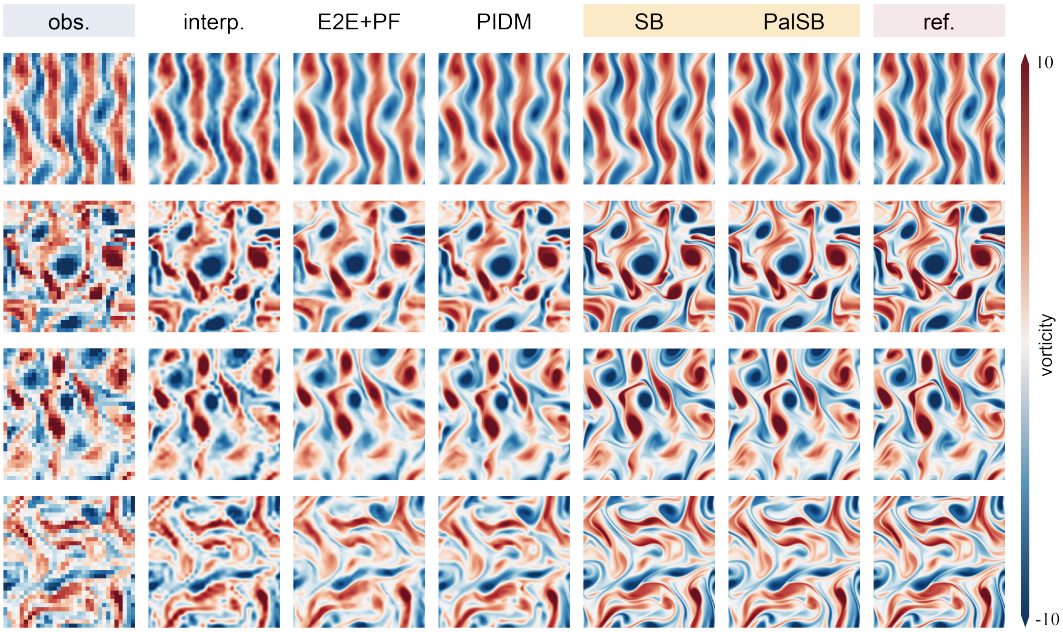

Figure 16: Additional results of Kolmogorov flow on FI task using noisy observations (8x super-resolution, 5% Gaussian noise).

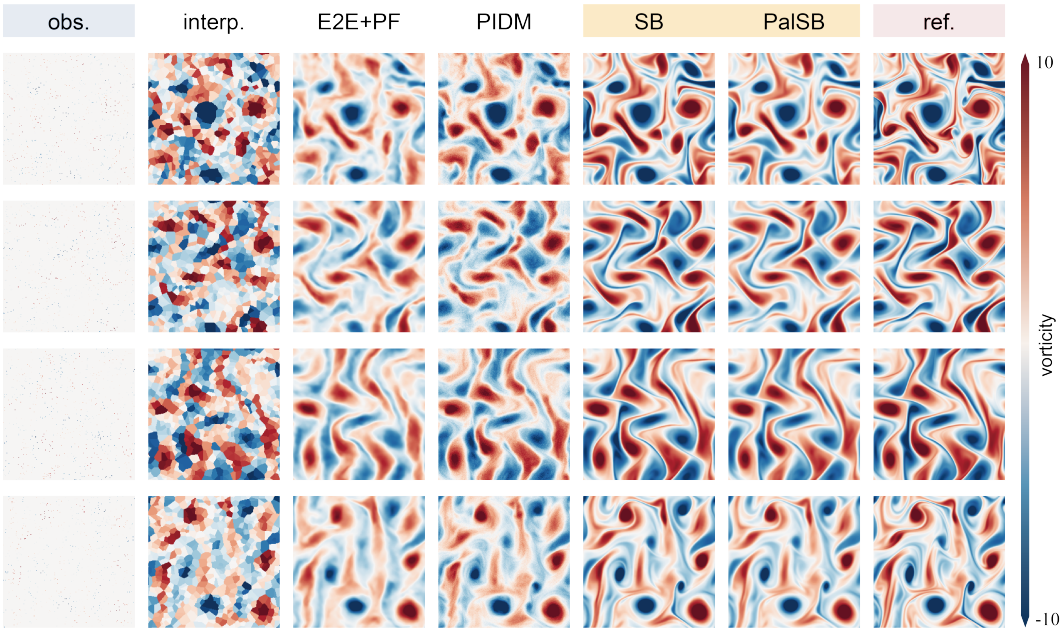

Figure 17: Additional results of Kolmogorov flow on RI task using noisy observations (99% masked, 5% Gaussian noise).

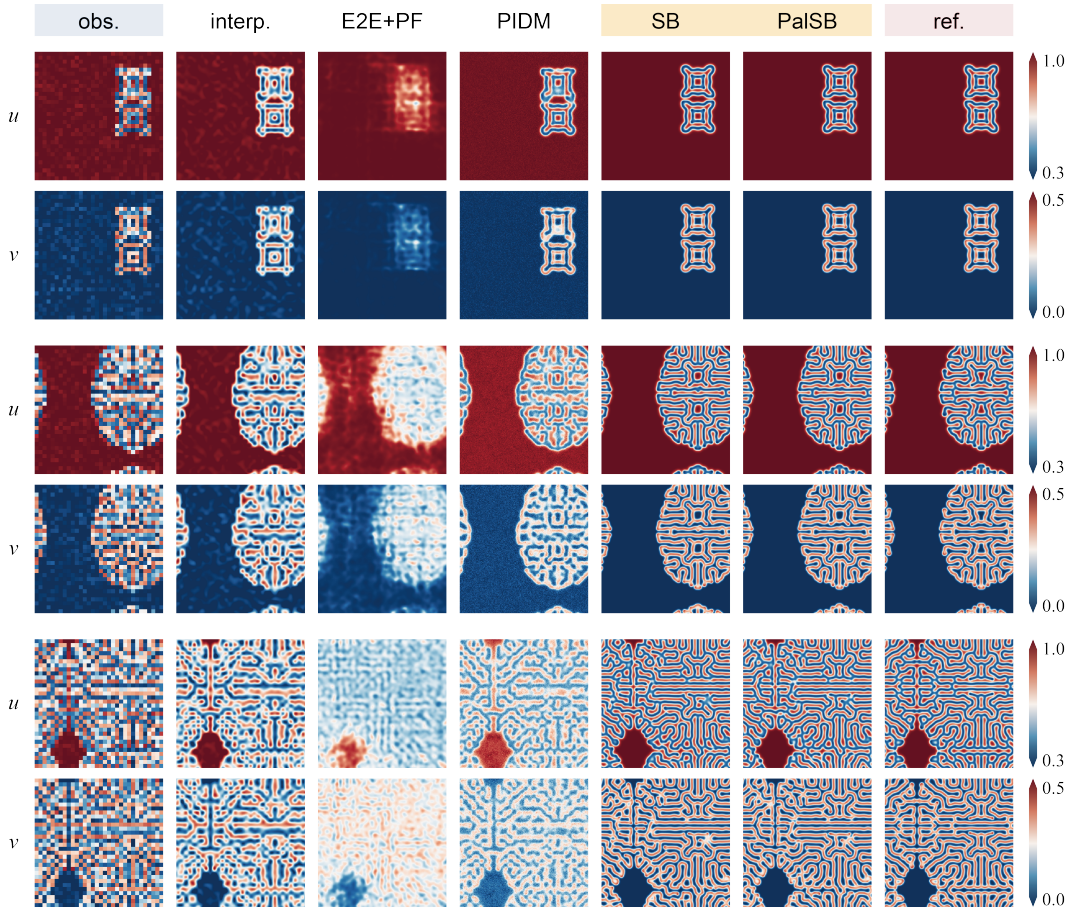

Figure 18: Additional results of GS-RD on FI task using noisy observations (8x super-resolution, 5% Gaussian noise).

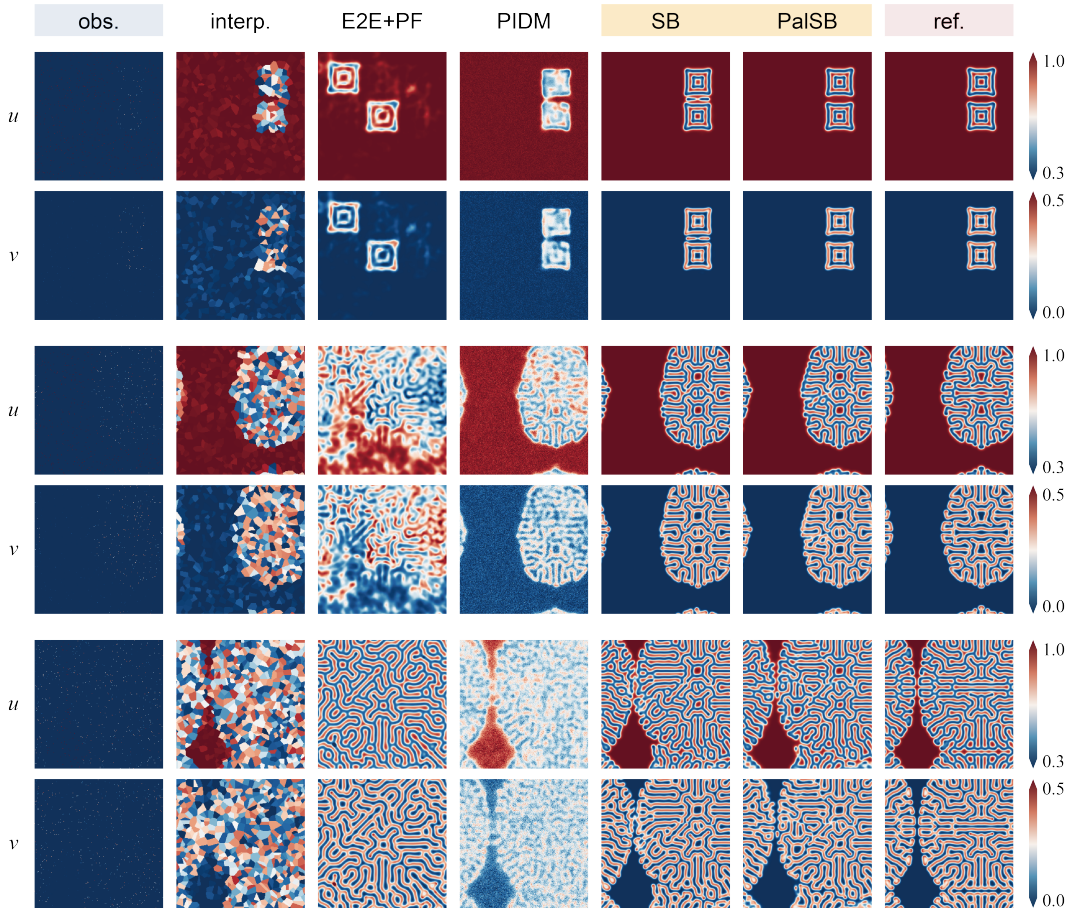

Figure 19: Additional results of GS-RD on RI task using noisy observations (99% masked, 5% Gaussian noise).

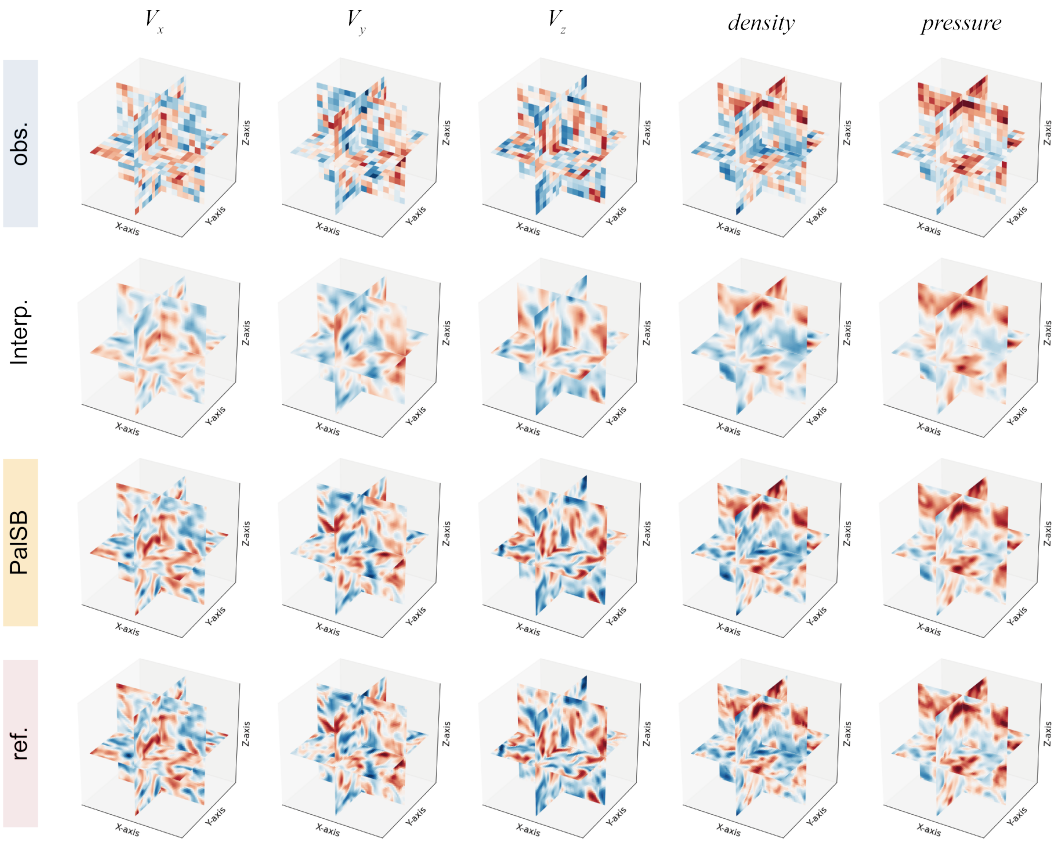

Figure 20: Extension on 3D case for FI task (4x super-resolution, noise-free).

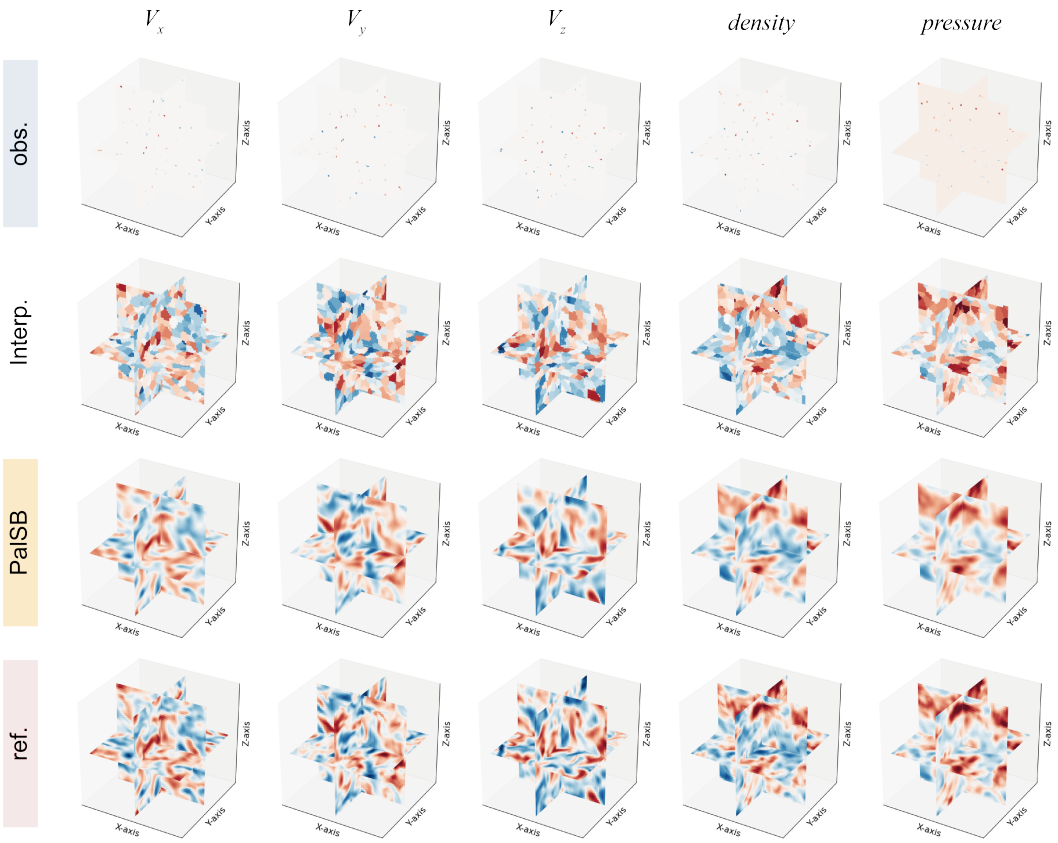

Figure 21: Extension on 3D case for RI task (99% masked, noise-free).

Table 6: Parameters of the neural network used in PalSB

Parameter name	Cylinder flow	Kolmogorov flow	Reaction-diffusion
Model architecture	DenoisingUNet Luo et al. (2023)	DenoisingUNet	DenoisingUNet
$\beta_{\min}$	0.1	0.1	0.1
$\beta_{\max}$	0.3	0.3	0.3
Number of scales	1000	1000	1000
Positional embeds	sinusoidal	sinusoidal	sinusoidal
Number of features	32	32	32
Channel multiplier	(1, 2, 4, 8)	(1, 2, 4, 8, 16)	(1, 2, 4, 8, 16)
Number of residual blocks	2	2	2
Nonlinearity	Swish	Swish	Swish
Dropout	0.1	0.1	0.1

Table 7: Parameters of FNO

Parameter name	Cylinder flow	Kolmogorov flow	Reaction-diffusion
Model architecture	2D FNO Li et al. (2020)	2D FNO	2D FNO
Modes 1	16	16	16
Modes 2	16	16	16
Number of features	32	32	32
Number of blocks	4	4	4
Nonlinearity	GeLU	GeLU	GeLU

Table 8: Parameters for training

Parameter name	Pretraining	Finetuning
Optimizer	AdamW	AdamW
Learning rate	1e-4	1e-5
Learning rate step	1000	10
Learning rate decay	0.99	0.99
Batch size	64	32
Small batch size	64	4
Number of iterations	100000	1000
Ema rate	0.995	-
Sampling steps T	-	10
Sampling step size	-	1e-3
Backpropogation steps B	-	1

Table 9: Loss weights for finetuning

Parameter name	Cylinder flow	Kolmogorov flow	Reaction-diffusion
γ_{phys}	5	0.5	1e5
γ_{reg}	1	10	1